Bioactive Materials 43 (2025) 273–291

Contents lists available at ScienceDirect

Bioactive Materials

journal homepage: www.keaipublishing.com/en/journals/bioactive-materials

A microenvironment responsive polyetheretherketone implant with antibacterial and osteoimmunomodulatory properties facilitates osseointegration

Miao Chen [a,1], Yusen Qiao [a,1], Lei Yu [a,1], Wei Wang [a], Wentao Wang [a], Haifu Sun [a], Yaozeng Xu [a], Jiaxiang Bai [b,c,***], Jun Zhou [a,**], Dechun Geng [a,c,*]

[a] Department of Orthopedics, The First Affiliated Hospital of Soochow University, Orthopedic Institute, Medical College, Soochow University, Suzhou, 215006, Jiangsu, China

[b] Department of Orthopedics, Centre for Leading Medicine and Advanced Technologies of IHM, The First Affiliated Hospital of USTC, Division of Life Sciences and Medicine, University of Science and Technology of China, Hefei, 230022, China

[c] National Center for Translational Medicine (Shanghai) SHU Branch, Shanghai University, Shanghai, China

ARTICLE INFO

Keywords:
Microenvironment responsive
Polyetheretherketone
Antibacterial
Immunomodulatory
Osseointegration

ABSTRACT

Failure of intraosseous prostheses is primarily attributed to implant loosening and infections. Current primary therapeutic modalities, such as antibiotics and local debridement, not only face challenges in thoroughly eliminating obstinate adhered bacteria but also encounter difficulties in ameliorating undue inflammatory reactions and regenerating impaired peri-implant bone tissues. Polyetheretherketone (PEEK) has excellent mechanical and physicochemical characteristics and has been used extensively as a medical biomaterial. However, the limited bactericidal and osseointegrative activities of bioinert PEEK restrict its clinical application. Herein, a microenvironment responsive coating with immobilised immunomodulatory magnesium ions (Mg^{2+}) and disinfectant cerium oxide nanoparticles (CNPs) is designed via ion coordination mediated by polydopamine (PDA) and electrospinning based on collagen structure-bionic silk fibroin (SF). By utilising the pH responsiveness of SF, CNPs exhibit potent antibacterial effects in an acidic environment (pH 5.0) caused by local bacterial infection. Due to the chelation interaction with PDA and the constraint of SF, Mg^{2+} is slowly released, ameliorating the local immune microenvironment and boosting osteogenesis by upregulating M2 phenotype macrophages. Bioinformatics analysis indicates that the inflammation is suppressed via the NF-κB signaling pathway. Overall, this SF-based coating maximizes the synergistic effect of CNPs and Mg^{2+}, offering enhanced antibacterial and osteoimmunomodulatory bioactivity for successful implantation.

1. Introduction

The prevalence of orthopedic implants is ascending owing to the global aging population and the associated increase in trauma and disease [1,2]. Metal implants, renowned for their remarkable mechanical strength, are the primary selection for hard-tissue substitutes to replicate physiological function [3–5]. Moreover, their high modulus of elasticity often triggers a stress-shielding effect, resulting in complications such as periprosthetic bone resorption and implant loosening [6,7]. Polyetheretherketone (PEEK), a thermoplastic material authorized by the Food and Drug Administration (FDA), exhibits an elastic modulus closer to that of human cortical bone than traditional implants, providing benefits, including favorable biocompatibility, light transmittance, frictional resistance, and chemical stability [8–11], making it a

Peer review under responsibility of KeAi Communications Co., Ltd.

* Corresponding author. Department of Orthopedics, The First Affiliated Hospital of Soochow University, Orthopedic Institute, Medical College, Soochow University, Suzhou, 215006, Jiangsu, China.

** Corresponding author.

*** Corresponding author. Department of Orthopedics, Centre for Leading Medicine and Advanced Technologies of IHM, The First Affiliated Hospital of USTC, Division of Life Sciences and Medicine, University of Science and Technology of China, Hefei, 230022, China.

E-mail addresses: jxbai1995@ustc.edu.cn (J. Bai), royf1@163.com (J. Zhou), szgengdc@suda.edu.cn (D. Geng).

[1] These authors contributed equally to this work.

https://doi.org/10.1016/j.bioactmat.2024.09.017

Received 17 June 2024; Received in revised form 8 September 2024; Accepted 12 September 2024

promising alternative to metallic materials. However, the inherent bioinertia of PEEK contributes to inadequate bone integration and insufficient bacterial resistance, significantly hindering its clinical application [12,13]. Traditional strategies for PEEK modification (e.g., surface introduction with inorganic coatings, engineering of surface microstructures, doping of bioactive metal ions, and surface modification with biomolecules) predominantly focus on optimizing the osteogenic capacity [10,14,15]. However, these tactics ignore the fact that exogenous biomaterials tend to trigger an uncontrolled local immune response, resulting in implant failure, as the implant may not be fully adapted to the *in vivo* microenvironment [16].

The immune microenvironment significantly influences biomaterial-related immune responses and bone tissue formation [17,18]. Macrophages, key effector cells in immune responses, exhibit a dynamic balance and can polarize into inflammatory macrophages (M1) or anti-inflammatory macrophages (M2) under various signaling stimuli, which are crucial for tissue-implant interactions [19–22]. Efficient and timely conversion of M1 macrophages to M2 macrophages is crucial for tissue healing and osseointegration surrounding bone implants [23,24]. M2 macrophages suppress inflammation, activate osteoprogenitor cells, and promote osteogenesis, creating a favorable osteoimmune environment by releasing anti-inflammatory (e.g., IL-10) and pro-osteogenic (e.g., VEGF and BMP-2) cytokines [20,25–27]. As a human body trace element, magnesium (Mg) plays a pivotal role in perpetuating local microenvironment homeostasis, and Mg^{2+} is indispensable for balancing bone metabolism and regulating human immunity [28,29]. For instance, Qiao et al. constructed a Mg^{2+}-modified nanostructured titanium surface to modulate the macrophage-mediated inflammatory response for improved osseointegration [30]. Notably, Mg^{2+} can ameliorate the pathological microenvironment, optimize immune function, and trigger beneficial cascading effects by regulating the transformation of macrophages toward the M2 subphenotype. This results in the release of cytokines and chemokines that support osteogenesis and foster a local immune microenvironment favorable for bone regeneration [30–32]. Unfortunately, Mg^{2+} lacks antimicrobial properties [33], yet early clearance of bacterial infections is indispensable prior to immunomodulation of the local microenvironment, as infections may be a persistent source of induced inflammatory responses that ultimately lead to implant failure [34].

Cerium oxide nanoparticles (CNPs) have garnered attention for their exceptional anti-infective properties, which minimize the risk of drug resistance through direct contact [35,36]. With low or no toxicity to mammalian cells, CNPs have sparked in-depth research in tissue antibacterial therapy [37]. However, the potential harm from excessive metal accumulation underscores the need for intelligent and controllable release systems. Silk fibroin (SF), a naturally active protein known for its exceptional biocompatibility, lack of toxicity, and degradability, has found applications in various delivery systems and orthopedic medical materials with osteogenic ability [38–41]. The architecture of SF, comparable to that of type II collagen, contributes to hydroxyapatite nucleation site generation and facilitates calcium deposition [42]. Moreover, SF undergoes alterations in charge and molecular conformation with changes in environmental pH, enabling the construction of a pH-responsive SF-based intelligent release system [43]. Accordingly, SF was employed to encapsulate CNPs, which were then electrospun onto the surface of the materials. The local infection microenvironment surrounding the implant tends to become acidic due to the organic acids produced by bacterial metabolism [44,45], prompting SF to exhibit a pH-responsive role. This allows for the rapid and large-scale release of CNPs precisely where bacteria appear, inhibiting unnecessary premature elution of metallic elements, thereby reducing toxicity and preventing the emergence of bacterial drug resistance.

In this work, polydopamine (PDA) was introduced onto the surface of sulfonated PEEK to boost its polymerization and binding properties through the oxidative self-polymerization of dopamine (DA) at pH 8.5. Subsequently, a PDA-based engineered supramolecular metal-phenolic network can be fabricated via intermolecular bonding between DA and immunoactive Mg^{2+}. Finally, SF encapsulated with antibacterial CNPs was used to construct a microenvironment-responsive electrospun membrane (Scheme 1a). This physicochemically reprogrammed surface engineering strategy can exhibit infection-triggered antibacterial effects against the acidic microenvironment surrounding the prosthesis and boost host immunomodulation, thus contributing to the establishment of a favorable bone-implant interface and preventing implant failure (Scheme 1b).

2. Results and discussion

2.1. Preparation and characterization of the implant coating

A microenvironment responsive PEEK biomaterial implant was manufactured by structuring a PDA coating chelated with Mg^{2+} on SP, followed by covering the surface with biomimetic and pH-responsive SF encapsulated with antibacterial CNPs through electrospinning. The surface geometry of the different specimens was detected by scanning electron microscopy (SEM) (Fig. 1a). Following sulfonation treatment, the PEEK surface developed a consistent three-dimensional (3D) porous architecture (noted as SP), which improved implant stability and bone regeneration. Subsequently, the obtained surface was immersed in a dopamine hydrochloride solution to form a PDA layer (noted as SPP), and SEM observation revealed that the original pores were partly covered. This difference may be related to our deliberate prolongation of the reaction time to augment the density of the coating [46], keeping bacteria from inhabiting the porous structure, leading to implant failure and providing a better platform for secondary reactions and functionalization [47]. The Mg^{2+} coating was covered using the same method and observed through SEM (noted as SPPMg), and the surface morphology did not change significantly. Finally, SF doped with CNPs was spun onto the surface through electrospinning (noted as SPPMg@Ce). A dense filamentous material can be clearly observed on the surface, but the morphology of the electrospun material was not obviously influenced by the addition of CNPs. Transmission electron microscopy (TEM) images further revealed that the particle size of the CNPs was less than 20 nm, with a mean size of 11.95 ± 3.14 nm (Fig. S1, Supporting Information).

The surface roughness (Ra) of PEEK increased considerably after sulfonation (Ra: 36.20 ± 4.53 and 95.66 ± 7.97 nm), while the surface microroughness of the SPP and SPPMg samples was relatively low (Ra: 27.20 ± 3.54 and 45.30 ± 6.08 nm) and more uniform. The surface roughness of the SPPMg@Ce samples after electrospinning was greater (Ra: 148 ± 14.71 nm) (Fig. 1b and c). Fig. 1d, e revealed the water contact angles of the various specimens. The hydrophobicity of the porous structure after sulfonation treatment slightly increased the contact angle of SP. The hydrophilicity of PDA was suggested to be the cause of the abrupt reduction in the water contact angle of SPP. The water contact angle of SPPMg did not change significantly after the introduction of Mg^{2+}. The contact angle further decreased after the incorporation of SF doped with CNPs, demonstrating that the surface hydrophilicity of SPPMg@Ce was superior to that of the other samples. This could be explained by the intricate chemical makeup of SF, which contains hydrophilic groups such as amine, carboxyl, and hydroxyl groups that cause polymer polarity [48]. In addition, improving the hydrophilicity of the biomaterial surface is promising to boost cell adhesion and the integration of the implant and surrounding bone tissues. Fig. 1g demonstrated the chemical composition of every functional group determined by X-ray photoelectron spectroscopy (XPS). We detected apparent peaks of C 1 s and O 1 s in the PEEK and SP samples. In addition, N 1 s signals were observed for all the substrates modified with PDA due to the high nitrogen content in the PDA. In SPPMg and SPPMg@Ce, high-resolution Mg 1 s and Ce 1 s peaks, respectively, were detected in the sample. The energy-dispersive X-ray spectrometry (EDS) results also verified this point (Fig. 1f, Fig. S2, Supporting Information).

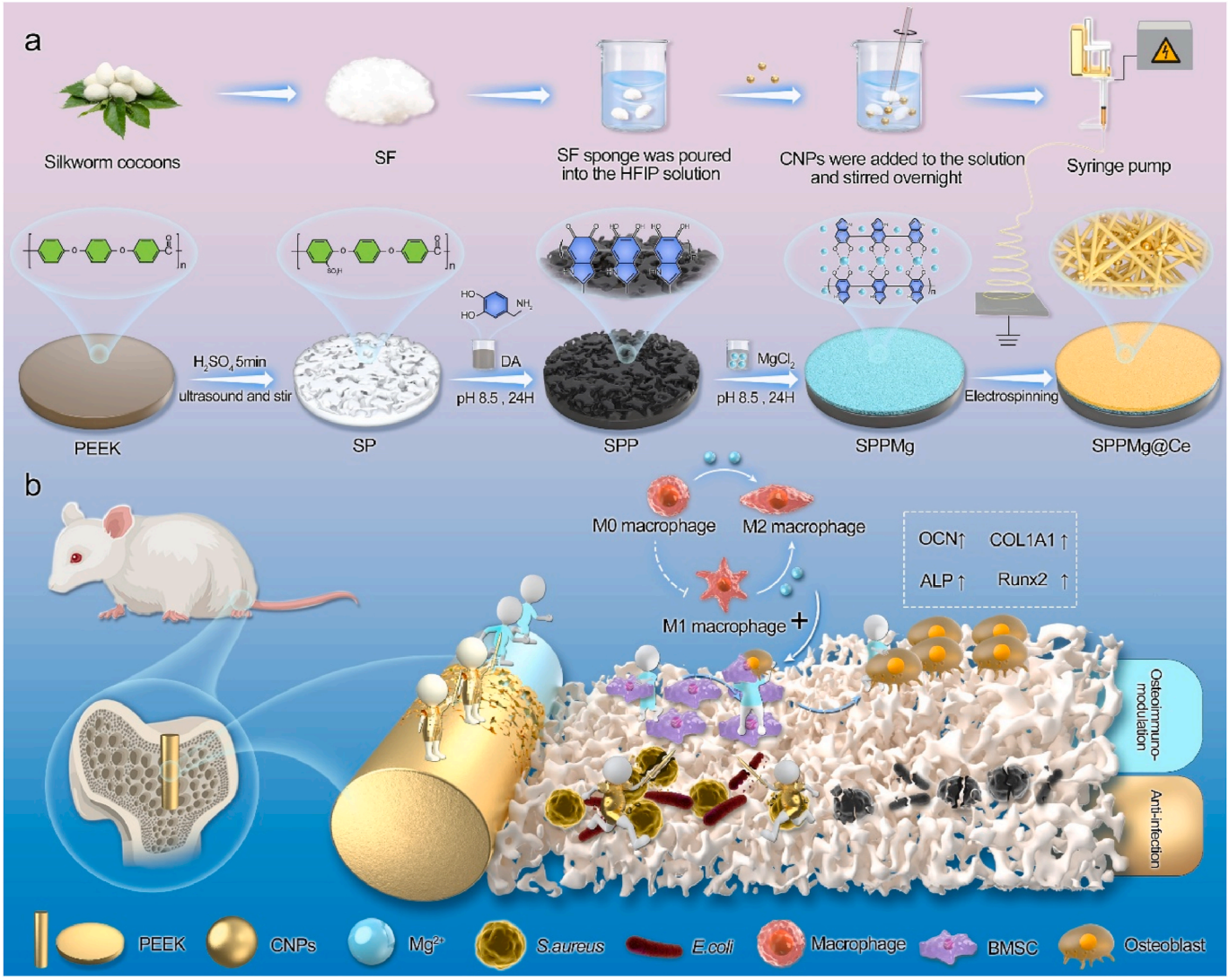

Scheme 1. Schematic illustration of SPPMg@Ce synthesis and its biomedical applications. a) The synthetic route of SPPMg@Ce multifunctional biomaterials. b) The PEEK modified with Mg^{2+} and CNPs demonstrates dual effects on osteoimmunomodulation and anti-infection *in vivo*, effectively ameliorating interfacial osteogenesis and osseointegration around bone implants.

PEEK possesses a comparatively low modulus of elasticity, comparable to that of cortical bone, which helps to avoid stress shielding [9]. The force–displacement curve of each sample was shown in Fig. 1h, and there was no apparent distinction amongst the five groups, demonstrating that the modified PEEK can still maintain an elastic modulus comparable to that of cortical bone and serve to avoid stress shielding. Notably, the stable bonding between the surface coating and the PEEK substrate is critical because the coating needs to function in the frictional environment of surgery or body motion. Herein, we placed prepared SPPMg@Ce samples under the skin of rats and removed them immediately or 10 days later. The EDS results showed that the functional coating was well conserved, demonstrating dependable bonding and long-term consistency of the integrated coating (Fig. S3, Supporting Information).

Regarding the loading amounts of CNPs and Mg^{2+}, it can be determined using inductively coupled plasma-optical emission spectrometer (ICP-OES) by measuring the changes in elemental content before and after the material preparation process. After calculation, the loading amount of CNPs and Mg^{2+} was 0.87 mg/cm^2 and 4.07 mg/cm^2, with loading efficiency of 85.24 % and 62.47 %, respectively. The release curves of the CNPs are displayed in Fig. 1i. Notably, due to the inherent characteristics of SF, burst and pH-responsive release of CNPs was observed. Specifically, the release amount almost reached its peak on approximately the second day. After 28 days, only 11.3 ppm of CNPs were released into PBS at pH 7.4, while 29.3 ppm and 24.5 ppm of CNPs were discharged at pH 5.0 and 6.0, respectively. In contrast, the ion coordination and physical isolation of SF mediated the sustained discharge of Mg^{2+}, and the release did not fluctuate significantly due to changes in pH (Fig. 1j). In summary, this coating successfully provided pH-responsive and sustained release, consequently implementing on-demand release of CNPs and Mg^{2+}.

2.2. *In vitro* cytocompatibility

Considering that cell compatibility is a prerequisite for implanting biomaterials, we studied SPPMg@Ce to validate its potential in biomedical applications through its cytotoxicity, cell adhesion, and cell proliferation impacts on RAW264.7 cells and bone marrow mesenchymal stem cells (BMSCs). The toxicity of the material to RAW264.7 cells and BMSCs was determined using live/dead staining. In the SPPMg@Ce group, fewer red fluorescent positively stained cells were observed, indicating a decrease in the number of dead cells (Fig. S4, Supporting Information). These findings illustrated that SPPMg@Ce has excellent biocompatibility. Cytotoxicity was also measured through

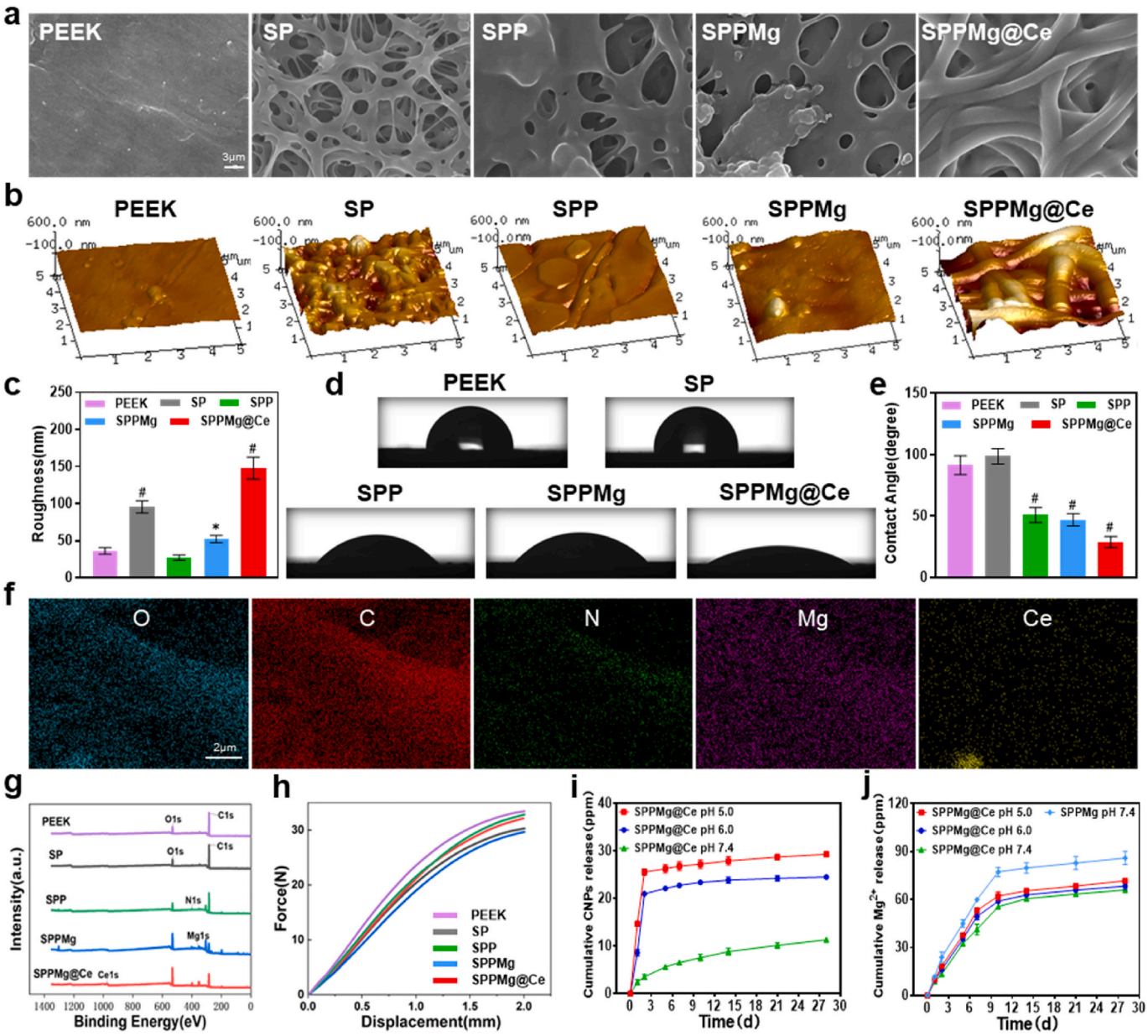

Fig. 1. Characterization of the integrated PEEK implants. a) Surface morphology SEM photographs of PEEK, SP, SPP, SPPMg and SPPMg@Ce. Scale bars: 3 μm. b) AFM images of the different modified surfaces. c) Surface roughness according to the AFM analysis. d, e) Morphologies and water contact angle droplets. f) EDS elemental mapping of SPPMg@Ce. Scale bar: 2 μm. g) XPS spectra of various PEEK specimens. h) Force–displacement curves of different PEEK samples. i) Release behavior of CNPs from SPPMg@Ce samples in terms of the cumulative release amount. j) Release behavior of Mg^{2+} from SPPMg and SPPMg@Ce in cumulative release amount. n = 3 biologically independent experiments, and statistical analysis was obtained leveraging one-way ANOVA. Data are expressed as mean ± SD, *p < 0.05 and #p < 0.001.

CCK-8 analysis (Fig. S5, Supporting Information). The cells in the SPPMg and SPPMg@Ce groups exhibited greater activity than did the other specimens, indicating that the release of metal ions ameliorated RAW 264.7 cell and BMSC proliferation. Overall, these results indicate that SPPMg@Ce has reduced potential cytotoxicity, excellent biocompatibility and biosafety. These positive outcomes would be instrumental in *in vivo* peri-implant tissue restoration, as predicted.

2.3. Evaluation of antibacterial performance in vitro

Biomedical implants are thought to be critically important for their anti-infective qualities because bacteria can attack the implant tissue interface, and unmanageable implant infections constantly lead to implant failure and necessitate replacement. Previous strategies to achieve implant antimicrobial activity through the construction of coatings generally failed to target the microenvironment of bacterial infections [8,15,49–51]. This low sensitivity and non-specificity may lead to poor sterilization efficacy and miss the optimal therapeutic window, while on the other hand, there is a concomitant possibility of over-treatment resulting in unnecessary drug toxicity damage. Therefore, we intend to construct pH-responsive smart antibacterial implants endowed with sensitive infection detection capabilities to overcome the dilemma of previous approaches.

Therefore, gram-negative *Escherichia coli* (*E. coli*) and gram-positive *Staphylococcus aureus* (*S. aureus*) served as model bacteria for assessing the antibacterial efficacy of different PEEK substrates [52]. The materials' antimicrobial effectiveness against *E. coli* and *S. aureus* was further assessed by employing the spreading plate method (SPM), and the

antibacterial rate was determined by quantifying the amount of bacterial colony-forming units (Fig. 2a–e, f). For the PEEK and SP samples, no obvious bactericidal effect was found, regardless of the pH. The survival rates of *E. coli* and *S. aureus* in the SPP group decreased to approximately 65 % at pH = 7.4, and there was no significant change when the pH decreased. After the introduction of Mg^{2+}, there was some improvement in the antibacterial effect, but the effect was limited. Nevertheless, SPPMg@Ce demonstrated outstanding antibacterial efficacy, achieving rates of 80.9 % and 81.1 % against *E. coli* and *S. aureus*, respectively, at pH = 7.4, and 98.5 % and 98.3 %, respectively, at pH = 5.0. This finding underscored both the antibacterial impact and pH responsiveness of the synthesized substrates.

The shape and integrity of the adhering bacteria on various substrate surfaces were assessed by SEM (Fig. 2b and c). Normal spherical *S. aureus* and rod-shaped *E. coli* with intact bacterial walls were observed on the PEEK and SP substrates. Although SPP and SPPMg exhibited some antimicrobial effects in bacterial count experiments, only a decrease in bacterial count was confirmed without significant changes in cell structure. Upon the addition of CNPs to the PEEK substrate, bacterial matrices from *S. aureus* and *E. coli* clearly leaked, and the bacterial membranes were visibly deformed, especially at pH = 5.0. As shown in Fig. 2g, the O-nitrophenyl-β-D-galactopyranoside (ONPG) hydrolysis level in the SPPMg@Ce group significantly surpassed that in the other groups, confirming that the interaction of CNPs with bacteria led to cell wall impairment and β-D-galactopyranoside release. Moreover, protein leakage indicated that the CNPs targeted the bacterial membrane, disrupting the native structure and causing bacterial cytoplasmic outflux and metabolic disruption (Fig. 2h). Subsequently, we delved into the bacteriostatic efficacy of the biomaterials through 3D reconstructions of live/dead staining. As depicted in Fig. 2d, the PEEK group exhibited green staining, signifying intact bacterial biofilms, with a minor amount of red-stained bacteria observed on the surfaces of the SP and SPP samples. The SPPMg@Ce sample displayed widespread red fluorescence, demonstrating an elevated quantity of dead bacteria in superficial biofilm architecture, attributed to the outstanding antibacterial performance of the CNPs. Crystal violet staining displayed similar trends, with the SPPMg@Ce group disrupting the dense biofilm and causing substantial biomass damage. Moreover, the biofilms in the other groups remained structurally intact and mostly viable (Fig. S6, Supporting Information). These results indicated that the addition of CNPs could strengthen the sterilization capacity of the substrate against *E. coli* and *S. aureus*.

The antimicrobial efficiency primarily stems from the mechanical disruption induced by CNPs [53]. The strong electrostatic characteristics of CNPs are thought to be responsible for their antibacterial potential. Positively charged CNPs readily adhere to the surfaces of both gram-positive and gram-negative bacteria, exploiting electrostatic interactions with negatively charged bacterial cell walls. This interaction profoundly compromises cell integrity, leading to inactivation of cellular proteins, penetration of nanoparticles into the bacterial cell to inactivate bacterial enzymes, and ultimately, resulting in systemic disruptions within the bacteria's internal biological system, which in turn cause bacterial death. In addition, the satisfactory surface area-to-volume ratio, unique morphology, and inhomogeneous surface texture of CNPs may render the bacteria more susceptible to physical damage and cell wall deterioration [54]. In summary, the antibacterial properties of SPPMg@Ce biomaterials are clearly demonstrated.

Infections can evoke macrophage polarization toward the proinflammatory M1 phenotype, triggering inflammatory responses and causing bone loss [55,56]. Therefore, it is imperative to validate the anti-infective effects of these materials before exploring their osteoimmunomodulation properties. Given the remarkable antibacterial effects of SPPMg@Ce biomaterials against *E. coli* and *S. aureus*, we are prompted to delve further into their performance in enhancing the immune microenvironment and promoting bone integration.

2.4. Immunomodulation of SPPMg@Ce by regulation of the macrophage polarization phenotype

In addition to infection, exogenous biomaterials, such as foreign objects, can exacerbate local immune responses postimplantation, activating the proinflammatory M1 phenotype in macrophages. Prolonged M1 macrophage activation and the subsequent inflammatory cascade contribute to subsequent bone destruction [57]. Consequently, the osteoimmunomodulatory efficacy of macrophage polarization conversion is crucial, as the subphenotype transition from M1 to M2 fulfils a pivotal function in implant-associated bone healing and integration [20,58]. Regulating the increase in the M2/M1 macrophage ratio effectively alleviated the inflammatory microenvironment and promoted bone reshaping on implant surfaces [59]. To validate this Mg^{2+}-based modification on the modulation of the immune microenvironment, RAW 264.7 cells were inoculated on the modified surface, and an inflammatory environment was simulated using LPS (Fig. 3a). Representative SEM photographs of RAW264.7 cells inoculated on substrate surfaces without Mg^{2+} coordination (i.e., the PEEK, SP and SPP groups) demonstrated that the macrophages predominantly displayed a pancake-like morphology, but the macrophages exhibited an elongated shape on the SPPMg and SPPMg@Ce surfaces (Fig. S7, Supporting Information). The significant morphological transformation toward an elongated shape on the surfaces of SPPMg and SPPMg@Ce suggested a preliminary transformation in the macrophage subphenotype from M1 to M2 [16].

Immunofluorescence staining was applied to investigate whether the modified biomaterials induced macrophage polarization. As depicted in Fig. 3b and c, the fluorescence intensity of iNOS in the PEEK group was obvious, whereas in the SPPMg and SPPMg@Ce groups, the iNOS expression level decreased. Conversely, SPPMg and SPPMg@Ce remarkably elevated the expression of the M2 macrophage marker arginase-1 (Arg-1), indicating that SPPMg and SPPMg@Ce can induce M2 macrophage activation (Fig. 3d). To further validate the subphenotypes of the macrophages on these engineered specimens, flow cytometry was employed to quantify $CD86^+$ (M1) and $CD206^+$ (M2) expression. As detailed in Fig. 3e–h, the M1 macrophage proportions on the various PEEK samples exhibited the following trend: SPPMg@Ce (14.6 %) < SPPMg (18.0 %) < SPP (31.1 %) < SP (35.2 %) < PEEK (41.9 %). Conversely, the M2 macrophage proportion exhibited the opposite trend: SPPMg@Ce (30.2 %) > SPPMg (26.6 %) > SPP (12.3 %) > SP (10.3 %) > PEEK (7.65 %). SP and SPP appeared to have a certain regulatory impact on macrophage polarization, albeit to a limited extent. Furthermore, Mg^{2+}-based biomaterials exerted a conspicuous contribution to macrophage phenotypic switching.

Macrophages exert osteoimmunomodulatory effects by secreting and releasing cytokines. Specifically, M1 macrophages release proinflammatory mediators including interleukin 1 (IL-1), interleukin 6 (IL-6) and tumor necrosis factor α (TNF-α) to induce inflammation [60]. In contrast, M2 macrophages generate anti-inflammatory cytokines including interleukin 10 (IL-10) and interleukin 4 (IL-4) to relieve inflammation and boost tissue repair [61]. Hence, variations in inflammatory cytokine gene expression levels were detected via RT–qPCR. As depicted in Fig. 3i–k, compared to those in the PEEK group, proinflammatory cytokines (*Tnfa* and *Il1b*) were significantly downregulated in the SPPMg and SPPMg@Ce groups. Conversely, the expression of the anti-inflammatory cytokine *Il10* dramatically increased in the SPPMg and SPPMg@Ce groups. Therefore, the sustained release of Mg^{2+} from SPPMg@Ce increased the percentage of M2-polarized macrophages, facilitating a coordinated phenotypic switch. The mechanism of the immunoregulatory effects of SPPMg@Ce needs further proof. Additionally, the upregulation of osteogenic cytokines, such as *Bmp-2*, in M2 macrophages induced by Mg^{2+}-based materials underscored the need to monitor changes in osteogenic function-related biological information in subsequent research on the underlying mechanism involved (Fig. 3l).

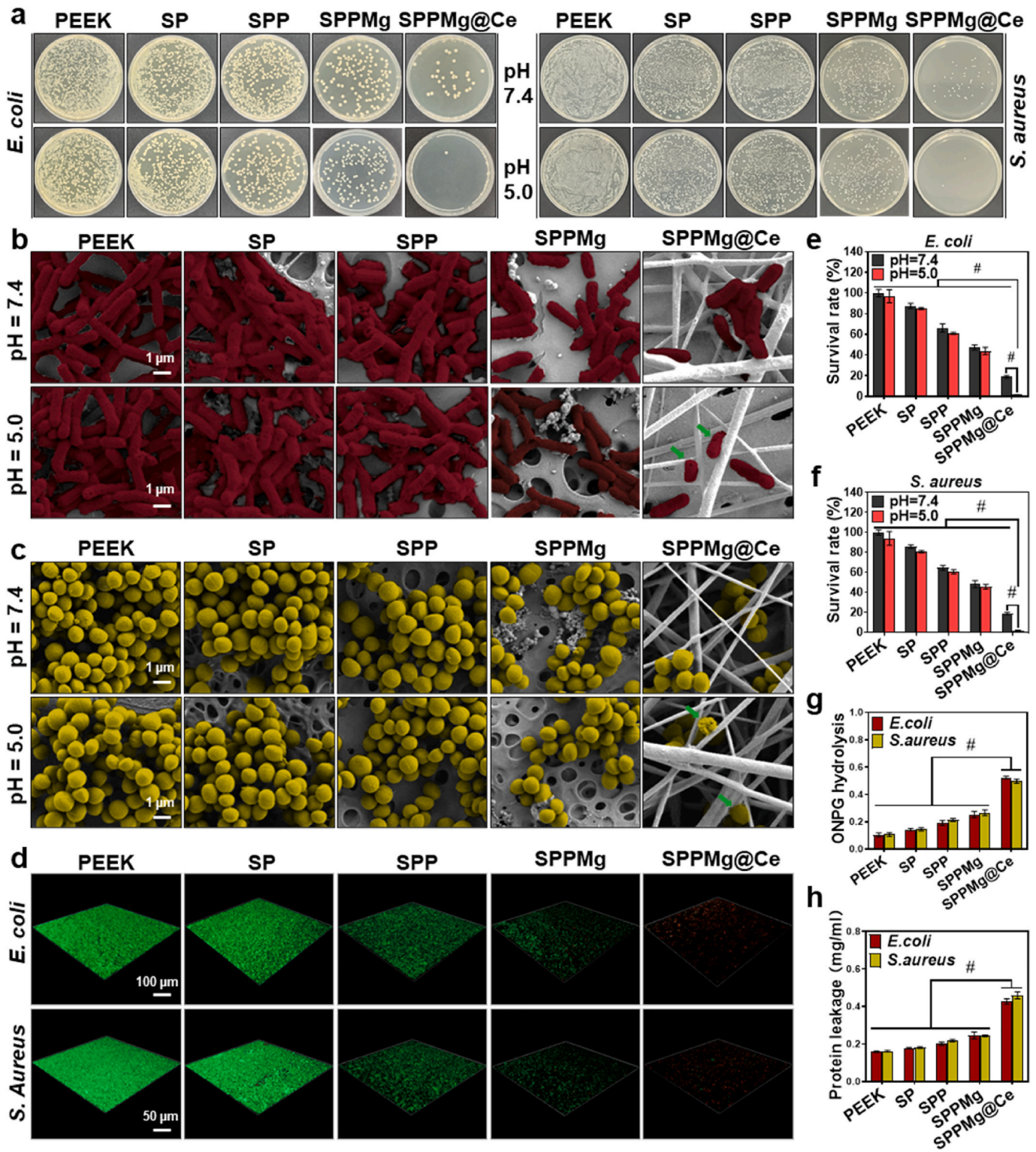

Fig. 2. Evaluation of antibacterial performance *in vitro*. a) Typical photos of SPM from *E. coli* and *S. aureus* after treatment with PEEK, SP, SPP, SPPMg and SPPMg@Ce. b, c) Representative SEM images of the various groups (the green arrows indicate destruction of the bacterial membrane). Scale bar: 1 μm; d) 3D reconstructions of the bacterial live/dead (Syto9/PI) staining of *E. coli* and *S. aureus* biofilms. Scale bars: 100 μm and 50 μm. e, f) Quantitative analysis relative to the SPM results. g) Membrane permeability detection by ONPG hydrolysis test of *E. coli* and *S. aureus* isolated from PEEK, SP, SPP, SPPMg and SPPMg@Ce. h) Protein leakage evaluation of *E. coli* and *S. aureus* after treatment with various PEEK specimens. n = 3 biologically independent experiments, and statistical analysis was obtained leveraging one-way ANOVA. Data are expressed as mean ± SD, $^{*}p < 0.05$ and $^{\#}p < 0.001$.

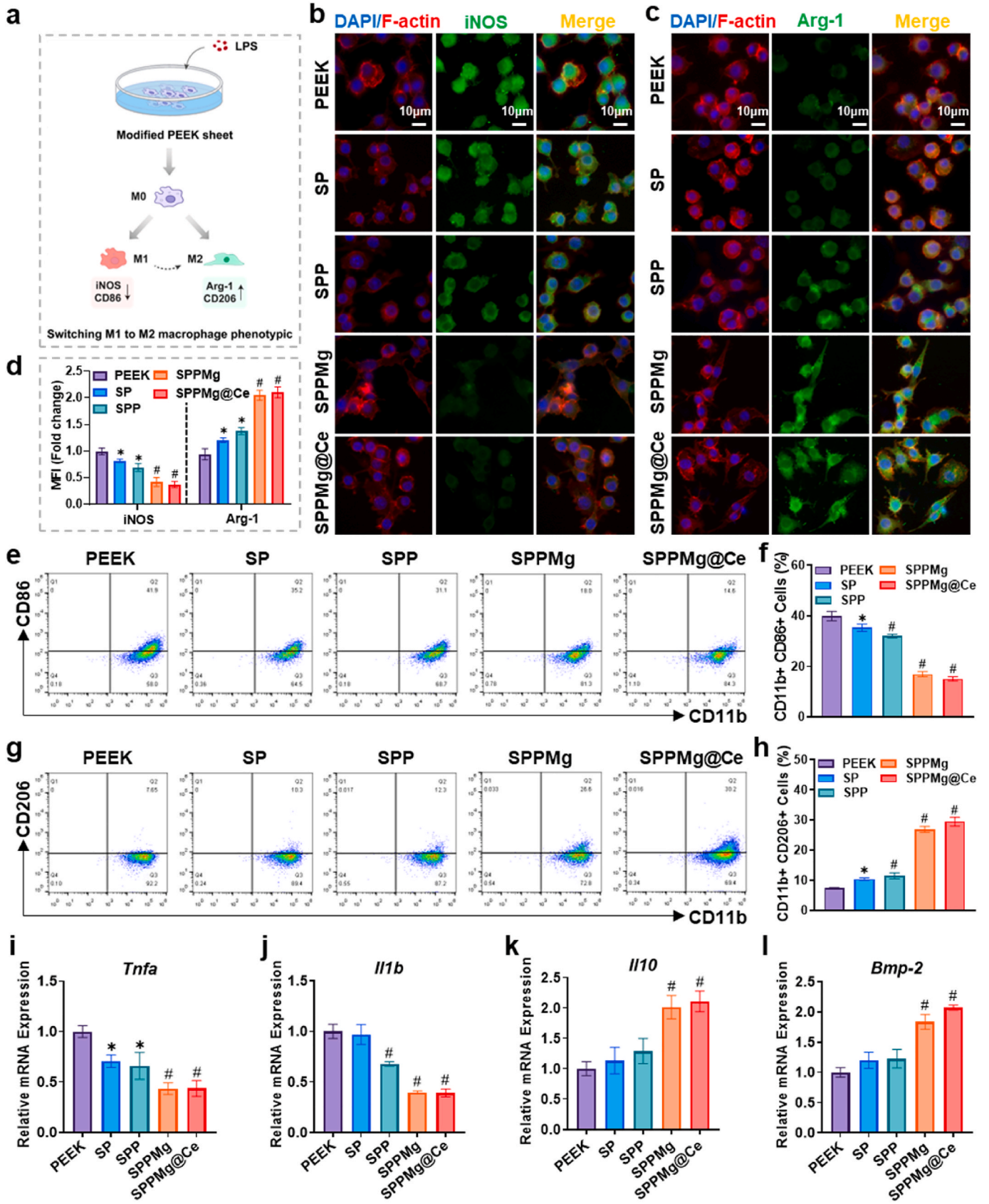

Fig. 3. Modified PEEK modulated macrophage polarization *in vitro*. a) Schematic diagram of experimental layout. b, c) Typical immunofluorescence staining results of RAW264.7 cells on PEEK, SP, SPP, SPPMg and SPPMg@Ce (green: iNOS or Arg-1; red: F-actin; blue: nuclei). Scale bar: 10 μm. d) Relative MFI quantification of immunofluorescence staining. e-h) Flow cytometry diagrams showing macrophage polarization. i-l) RT−qPCR results for *Tnfa*, *Il1b*, *Il10*, and *Bmp-2*. n = 3 biologically independent experiments, and statistical analysis was obtained leveraging one-way ANOVA. Data are expressed as mean ± SD, *p < 0.05 and #p < 0.001.

2.5. RNA-seq validation of the immunoregulatory mechanism

To further decipher the structure and function of the genome during the regulation of immunity by SPPMg@Ce and to identify alterations in relevant signaling pathways, RNA sequencing was conducted. The results demonstrated that SPPMg@Ce can downregulate the expression of genes relevant to the inflammatory reaction in macrophages in an LPS-induced inflammatory environment. These findings spurred us to delve deeper into the underlying mechanism and associated biological incidents of macrophage manipulation with SPPMg@Ce. Principal component analysis (PCA) illustrated good reproducibility among the sample groups, meeting the prerequisites for subsequent analysis (Fig. 4a). Differentially expressed genes (DEGs) analysis showed that 1415 DEGs were up-regulated, while 1402 DEGs were down-regulated in the SPPMg@Ce group versus the PEEK group (Fig. 4b). Heatmap analysis displayed pronounced distinctions in DEGs expressions across the two groups, indicating a substantial impact of SPPMg@Ce on macrophage gene expression (Fig. 4c).

DEGs analysis identified significant variations in thousands of genes across the PEEK group and the SPPMg@Ce group, prompting a more in-depth exploration of the induced changes in biological processes. Subsequently, GO enrichment analysis was conducted, highlighting immune and inflammatory reactions as major concerns in SPPMg@Ce-induced alterations (Fig. 4d). Particularly at the biological process level, in comparison with those in the PEEK group, the genes in the SPPMg@Ce group were predominantly associated with the negative regulation of the inflammatory response and immune response but positively modulated immune system processes and the innate immune response (Fig. S8, Supporting Information). The complexity of immune regulation is reflected in the differential expression of genes within the SPPMg@Ce group in the immune system. Genes that are upregulated may be pivotal in triggering the initial immune response, whereas those that are downregulated likely serve as part of negative feedback mechanisms to fine-tune and control the response. Kyoto Encyclopedia of Genes and Genomes (KEGG) pathway enrichment analysis demonstrated significant alterations of the TNF, NF-κB, Toll-like, IL-17 and BCR signaling pathways by SPPMg@Ce (Fig. 4e, Fig. S9, Supporting Information). Notably, all of these pathways are related to inflammation. For example, the IL-17 signalling pathway is associated with inflammation, autoimmune diseases and host defence, and IL-17 is a pro-inflammatory cytokine that mediates the pathogenesis of multiple inflammatory diseases and augments the pro-inflammatory phenotype of macrophages [62–64]. To further specify the relevant signalling pathways, Gene set enrichment analysis (GSEA) was carried out and the results revealed that the TNF and NF-κB pathways were inhibited in the SPPMg@Ce group, which was in agreement with the KEGG outcomes. (Fig. 4f and g). Additionally, representative DEGs in these two signaling pathways were also exhibited in a heatmap (Fig. S10, Supporting Information).

The NF-κB pathway serves as a classical inflammatory pathway that has been ascertained to be a pivotal promoter of proinflammatory M1 macrophage polarization and to participate in TNF signaling pathways. To assess its impact, the phosphorylation levels of IκBα and p65 were estimated via western blotting. The outcomes revealed that the phosphorylation levels of IκBα and p65 in the SPPMg@Ce group were markedly lower than that of the PEEK group and similar to that of the BAY 11–7082 group (an inhibitor of the NF-κB signaling pathway), indicating that SPPMg@Ce had the ability to suppress the NF-κB pathway and inhibit the mobilisation of relevant inflammatory pathways (Fig. 4h, Fig. S11, Supporting Information). Protein–protein interaction (PPI) network analysis further illuminated differences in proteins encoded by DEGs and explored their interaction relationships (Fig. S12, Supporting Information). In the SPPMg@Ce group, the protein network genes associated with the inflammatory response (Tnf and Il1b) were markedly downregulated, consistent with the GO and KEGG enrichment analyses. Notably, an increase in Usp2, which is crucial for PTH-induced osteoblast proliferation, was observed among the genes that interact with Tnf. Furthermore, GSEA indicated the inhibition of negative regulation of osteoblast differentiation in the SPPMg@Ce group (Fig. S13, Supporting Information), prompting further exploration of the impact of immune microenvironment changes on osteogenic function.

2.6. Evaluation of osteogenic differentiation in vitro

To assess the direct effects of the modified substrates on osteogenesis, BMSCs were initially cultured on various PEEK plates, followed by induction in conventional osteogenic medium. ALP and ARS staining were conducted at 14 and 21 days after induction, respectively, to assess the osteogenic differentiation capacity (Fig. S14, Supporting Information). These results confirmed that SPPMg and SPPMg@Ce significantly enhanced ALP activity and promoted matrix mineralization. Furthermore, compared to those in the other groups, immunofluorescence staining showed significantly greater expression of Runx2 in the SPPMg and SPPMg@Ce groups (Fig. S15, Supporting Information). The expression of genes relevant to osteogenesis (e.g., *Alp*, *Col1a1*, *Runx2*, and *Opn*) were examined using RT−qPCR (Fig. S16, Supporting Information). In contrast to the PEEK group, the Mg^{2+}-coated PEEK plate group demonstrated significantly greater expression levels of the related genes. Collectively, SPPMg and SPPMg@Ce displayed superior direct induction of osteogenesis.

Once implanted, numerous cells comprising immune cells and BMSCs are recruited towards the bone implant surfaces. Favorable crosstalk between immune and bone-forming cells is pivotal for mitigating inflammation and initiating new bone formation [65]. To investigate the modulation of osteogenic differentiation by macrophage cytokines, RAW 264.7 cells were inoculated onto various specimens to generate conditioned medium (CM). After that, the osteoimmunomodulatory function of the various groups was assessed by utilising macrophage CM for culturing BMSCs (Fig. 5a). Cytoskeletal immunofluorescence staining revealed that BMSCs in the PEEK group exhibited poor spreading and deficient cellular extension, while BMSCs in the SPPMg and SPPMg@Ce groups displayed improved cell adhesion, facilitating more complete cell spreading (Fig. S17, Supporting Information). ALP staining was performed on cells grown in CM for 14 days to assess the effectiveness of osteogenic differentiation (Fig. 5b). ALP activity levels were greater, and there were more ALP-positive cells in the Mg^{2+}-coated SPPMg and SPPMg@Ce groups than in the other groups (Fig. 5e and f). Then, on day 21, we assessed the mineralization ability by ARS staining. Fig. 5c illustrated few calcium crystals in the PEEK and SP groups, with more red-stained mineral nodules in the SPP group. However, the SPPMg and SPPMg@Ce groups exhibited significantly greater numbers and sizes of mineralized nodules than the other groups, as confirmed by absorbance detection after calcium salt dissolution (Fig. 5g). Runx2 immunofluorescence staining further validated the most efficient enhancement in the SPPMg and SPPMg@Ce groups during osteogenic induction of CM coculture (Fig. 5d–h). Similar trends were observed when we estimated the expression of osteogenesis-associated genes, specifically *Alp*, *collagen type I alpha 1 chain* (*Col1a1*), *Runt-related transcription factor 2* (*Runx2*) and *Opn* (Fig. 5i–l). The mRNA expression levels of osteogenesis-associated genes were notably greater in the SPPMg and SPPMg@Ce groups than in the other groups, proving the potent property of SPPMg and SPPMg@Ce to facilitate osteogenic differentiation. In essence, these findings suggested that the incorporation of immunoactive Mg^{2+} into samples orchestrated immunomodulatory osteogenesis in BMSCs. To further characterize the SPPMg group and the SPPMg@Ce group for boosting osteogenesis, we measured the concentration of Mg^{2+} in the CM in each group. Subsequently, we performed ARS staining, with the $SPPMg^{\#}$ and $SPPMg@Ce^{\#}$ groups receiving only respective Mg^{2+} intervention, while the $SPPMg^{CM}$ and $SPPMg@Ce^{CM}$ groups were treated with their respective CM. The results showed that the $SPPMg^{CM}$ group exhibited significantly greater numbers and sizes of mineralized nodules compared to the $SPPMg^{\#}$ group. A

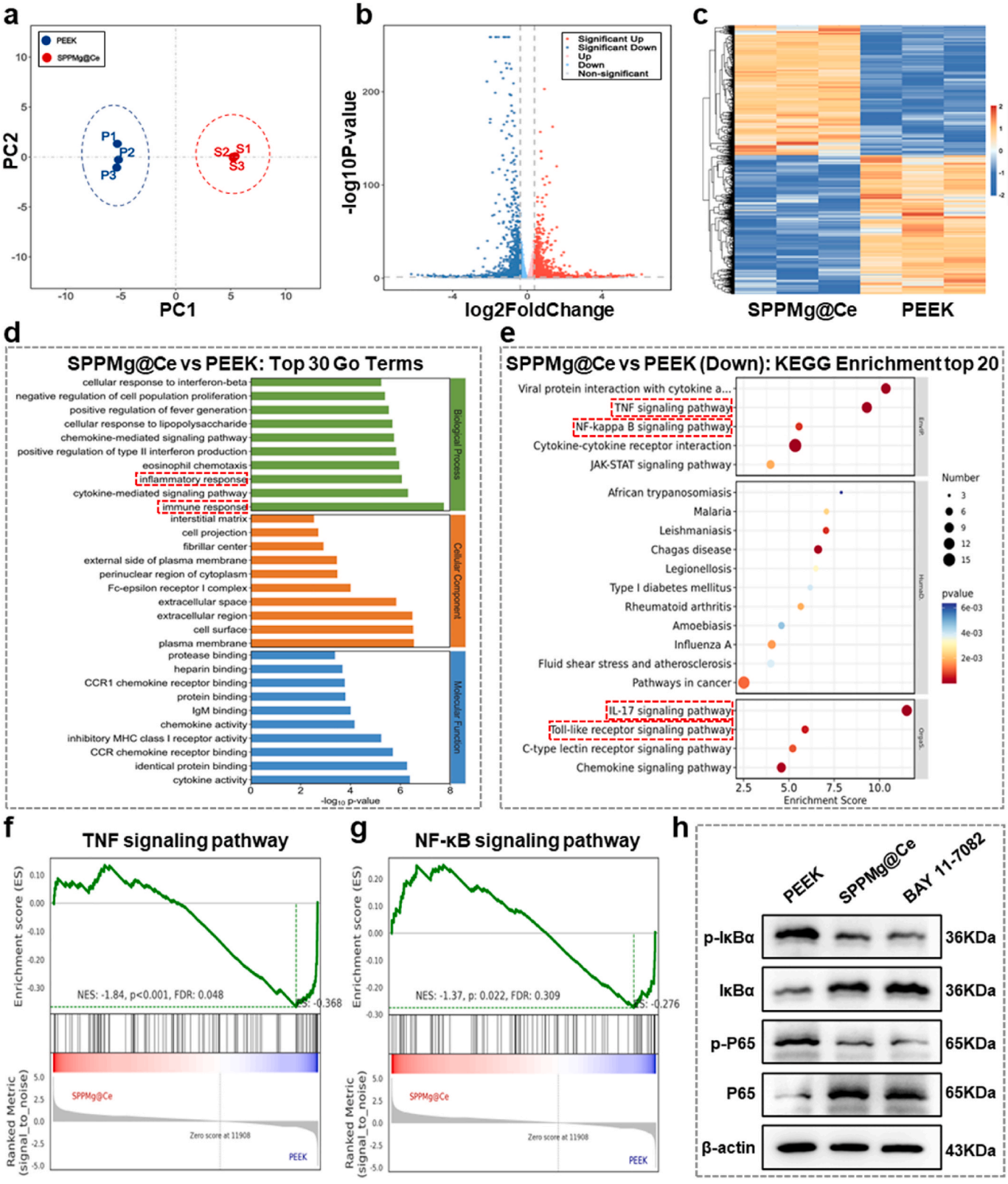

Fig. 4. Transcriptome sequencing analysis of the mechanism by which SPPMg@Ce modulated macrophage polarization. a) PCA of DEGs determined by RNA-seq in the PEEK and SPPMg@Ce groups. b) Volcano map of DEGs in the SPPMg@Ce group versus the PEEK group. c) Heatmap of DEGs. d) GO enrichment analysis of DEGs. e) KEGG enrichment analysis of DEGs. f, g) GSEA of the TNF and NF-κB signaling pathways. h) IκBα and P65 phosphorylation levels were assessed in the NF-κB signaling.

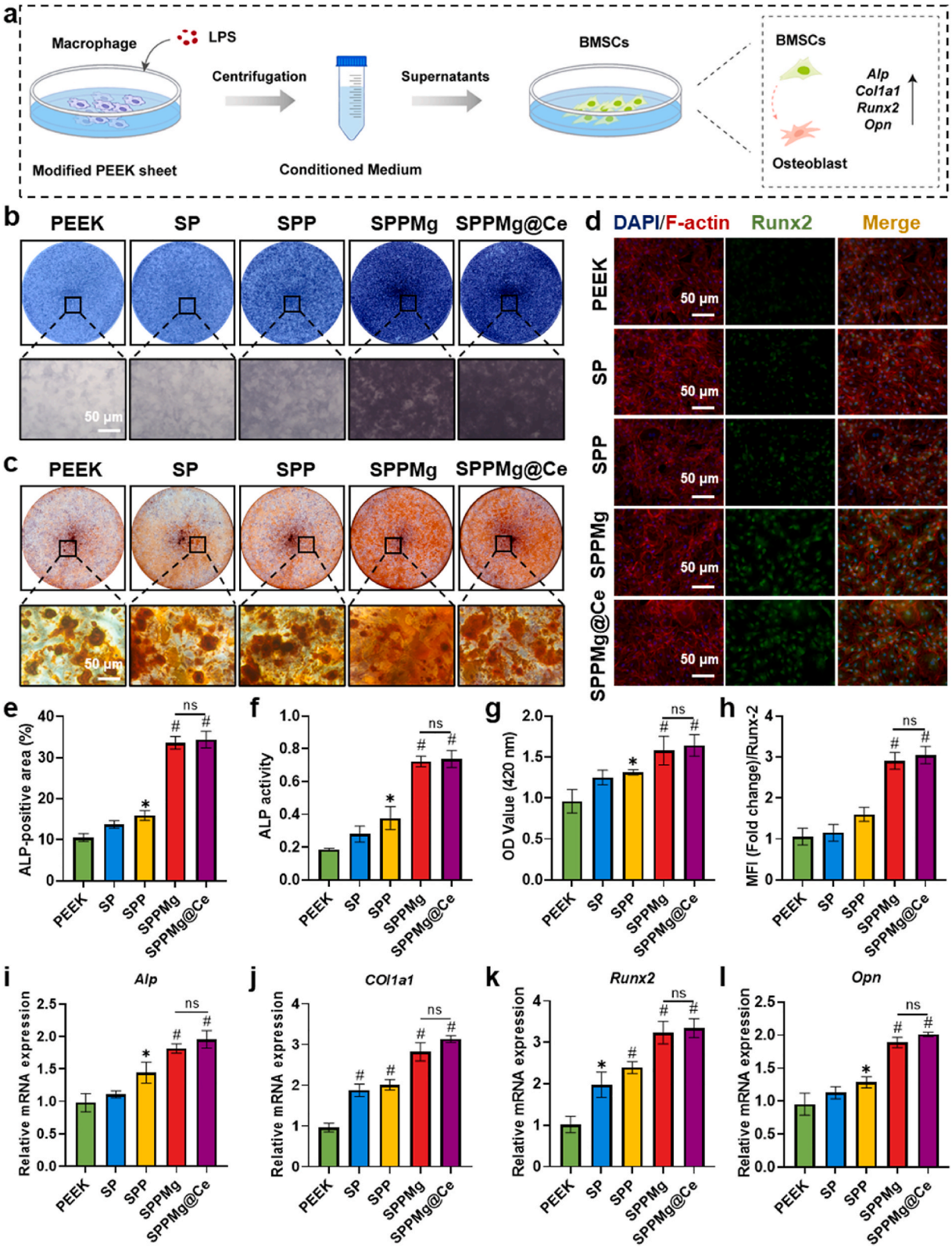

Fig. 5. Mg^{2+}-modified surfaces boosted osteogenic differentiation via immunomodulation. a) Schematic diagram of experimental layout. b) ALP staining of BMSCs nurtured in CM supplemented with osteogenic media. Scale bar: 50 μm. c) ARS staining of BMSCs nurtured in CM supplemented with osteogenic media. Scale bar: 50 μm. d) Photographs of BMSCs after immunofluorescence staining (green: Runx2; red: cytoskeleton; and blue: nuclei). Scale bar = 50 μm. e) ALP-positive cell/area (%) according to ALP staining. f) ALP activity of BMSCs in the PEEK, SP, SPP, SPPMg and SPPMg@Ce groups. g) Semi-quantitative analysis of the calcium nodule content in the various groups. h) Relative MFI quantification of immunofluorescence staining. i–l) Osteogenesis-associated gene expression in BMSCs nurtured in CM determined by RT–qPCR (*Alp, Col1a1, Runx2 and Opn*). n = 3 biologically independent experiments, and statistical analysis was obtained leveraging one-way ANOVA. Data are expressed as mean ± SD, ns: p-value >0.05, *$p < 0.05$ and $^{\#}p < 0.001$.

similar trend was observed in the comparison between the SPPMg@Ce^{CM} and SPPMg@Ce$^{\#}$ groups (Fig. S18, Supporting Information), indicating that the CM demonstrated superior osteogenic effects compared to the addition of Mg^{2+} alone. This was achieved by fostering the transformation of macrophages into the M2 subphenotype, generating an optimal osteoimmunomodulatory microenvironment through the interplay between reparative and osteogenic cytokines, thereby facilitating immuno-enhanced osteogenesis. In summary, SPPMg and SPPMg@Ce not only mediate macrophage subphenotypic transformation, but also enable direct osteoinduction, synergistically generating a microenvironment conducive to bone regeneration.

2.7. Evaluation of antibacterial activity in vivo

Inspired by the extraordinary bacterial eradication performance of SPPMg@Ce *in vitro*, we established a rat subcutaneous infection model to visually investigate its early antibacterial properties *in vivo*. The detailed procedure of the subcutaneous infection model was illustrated in Fig. S19, Supporting Information. Specifically, following implant insertion, a microsyringe was used to inject 100 μL of PBS containing *S. aureus* (1×10^7 CFU/ml) onto the specimen surface to minimize bacterial suspension leakage. Fig. 6a depicted the morphological changes and healing outcomes of the skin tissues over the 10-day treatment period. Notably, skin swelling and suppuration were detected in the PEEK, SP, and SPP groups, implying that bacterial infection in the abscess area caused an inflammatory response. The SPPMg group exhibited moderate swelling of scabby skin tissue, suggesting that Mg^{2+} had limited antibacterial effects. In contrast, the SPPMg@Ce group exhibited no obvious swelling, purulence, or wound ulceration, indicating that it had the most effective antibacterial capacity. As depicted in Fig. 6b, a substantial amount of pus was detected on the gross specimens in the PEEK and SP groups. While no obvious pus macroscopically remained on the SPP or SPPMg sheets, swelling of the local skin tissues was still evident. Conversely, the SPPMg@Ce group displayed a notable reduction in residual pus on the implant surfaces, accompanied by relieved tissue swelling. The medium of the bare PEEK group exhibited more turbidity than did the medium of the other groups, whereas the medium in the SPPMg@Ce group was the clearest and most transparent, consistent with the spreading plate method results. Additionally, the quantity of colony-forming units (CFUs) was estimated by assessing ultrasonic lysates of bacterial residues on PEEK plates and subcutaneous tissue homogenates of the peri-implant tissues. As anticipated, in comparison with the other four groups, the SPPMg@Ce group had a significantly smaller number of bacterial colonies (Fig. 6c and d), which further substantiated the exceptional antimicrobial properties of SPPMg@Ce. In addition, the peripheral tissues of the infected areas were harvested for histomorphological and quantitative analyses on day 10 after implantation.

Hematoxylin and eosin (H&E) staining exhibited a large remnant of neutrophil infiltration in the PEEK group, together with the widest infiltration range, suggesting an inflammatory response caused by infection (Fig. 6e and f). Meanwhile, the inflammation was slightly attenuated and the infected tissues were marginally repaired in the SP, SPP and SPPMg groups. In contrast, H&E-stained images showed standard follicle formation with no marked neutrophil infiltration in the SPPMg@Ce group. Furthermore, Giemsa staining revealed abundant bacterial colonies in the control group (Fig. 6g), confirming bacterial infiltration in the PEEK group. Conversely, nearly no bacteria were observed in the SPPMg@Ce group, indicating that bacterial invasion from the topical tissues was considerably eliminated. In summary, we have demonstrated that the SPPMg@Ce material exhibits prominent antibacterial properties *in vivo* and effectively combats issues related to implant infection.

2.8. Macrophage phenotypic transformation in vivo

The phenotypic transition of macrophages exerts a fundamental function in bone healing and implant osseointegration [20]. This is linked to macrophage deformability, which is vital for early neo-bone formation during inflammation. Considering the regulation of the immune microenvironment and osteogenic function by macrophages *in vitro*, immunomodulatory activity and osteogenicity *in vivo* were further explored. Using a standard surgical protocol, PEEK rods were embedded into the femoral condyles of the rats. Postimplantation, inflammation is inevitable and has inherent merits, whereas sustained release of proinflammatory cytokines secreted by M1-phenotype macrophages exacerbates chronic inflammation and impairs osseointegration [66], ultimately leading to prosthetic failure.

First, we collected animal skeletal tissues for detection in the initial phase of modeling, as macrophages mainly exhibit immunoregulatory functions at this time. H&E staining revealed that the SPPMg and SPPMg@Ce groups exhibited milder inflammatory responses in the tissues near the prosthesis than did the other groups, along with enhanced structural integrity of the bone in proximity to the prosthesis. In contrast, extensive infiltration of inflammatory cells and the presence of deteriorating bone structures adjacent to the bare PEEK implant suggested these as primary factors contributing to implantation failure (Fig. 7a–d). Immunofluorescence staining was further conducted to assess macrophage phenotypic transformation. Inflammatory infiltration was ascertained by labeling with CD68, and the conversion of M1 to M2 macrophages was probed by labeling with iNOS and Arg-1 (Fig. 7b). Immunofluorescence images demonstrated that iNOS-positive cells surrounding the bare PEEK rod were significantly more abundant than others, while the SPPMg and SPPMg@Ce groups exhibited the lowest quantity of macrophages with iNOS-positive staining near the materials (Fig. 7e). In contrast, more Arg-1-positive cells were observed in both the SPPMg and SPPMg@Ce groups versus the other groups (Fig. 7f). Similar trends were observed via immunohistochemical staining (Fig. 7c). The distribution of IL-10, an anti-inflammatory cytokine, was substantially elevated around the peri-implant regions in the SPPMg and SPPMg@Ce groups (Fig. 7h), while the proinflammatory cytokine TNF-α was considerably lower in these groups than in the PEEK group (Fig. 7g). These results, combined with a reduced number of infiltrating inflammatory cells and a shift in the macrophage subphenotype toward a favorable immune microenvironment, confirmed that SPPMg and SPPMg@Ce could alleviate the overactivation of proinflammatory macrophages triggered by tissue damage. Additionally, modified Mg^{2+}-based biomaterials enhanced the shift of macrophages from the M1 to M2 subphenotype *in vivo*, hence modulating the local immune environment and improving interfacial osseointegration around the implants.

2.9. Osseointegration in vivo

Implantable biomaterials with exceptional osteoimmunomodulatory performance can optimize the osteoimmune environment, accelerate osteogenic differentiation and neo-bone formation and ameliorate bone integration [25]. Having confirmed the potent immunoactivity of SPPMg@Ce in modulating macrophage polarization and facilitating osteogenic differentiation *in vitro*, along with its ability to transform the macrophage subphenotype from M1 to M2 *in vivo*, we investigated whether SPPMg@Ce could enhance osseointegration at the implant-to-bone interface *in vivo*. Bone tissues were harvested from the experimental rats for further evaluation 8 weeks after the operation. According to the 3D reconstructions of the micro-CT outcomes, after implantation of pure PEEK rods, the generation of new bone surrounding the prosthesis was minimal. In comparison with those in the bare PEEK group, more new bone was noted in the SP group and SPP group, which was generated by the construction of porous structures and the enhancement of PDA in the proliferation and adhesion of BMSCs,

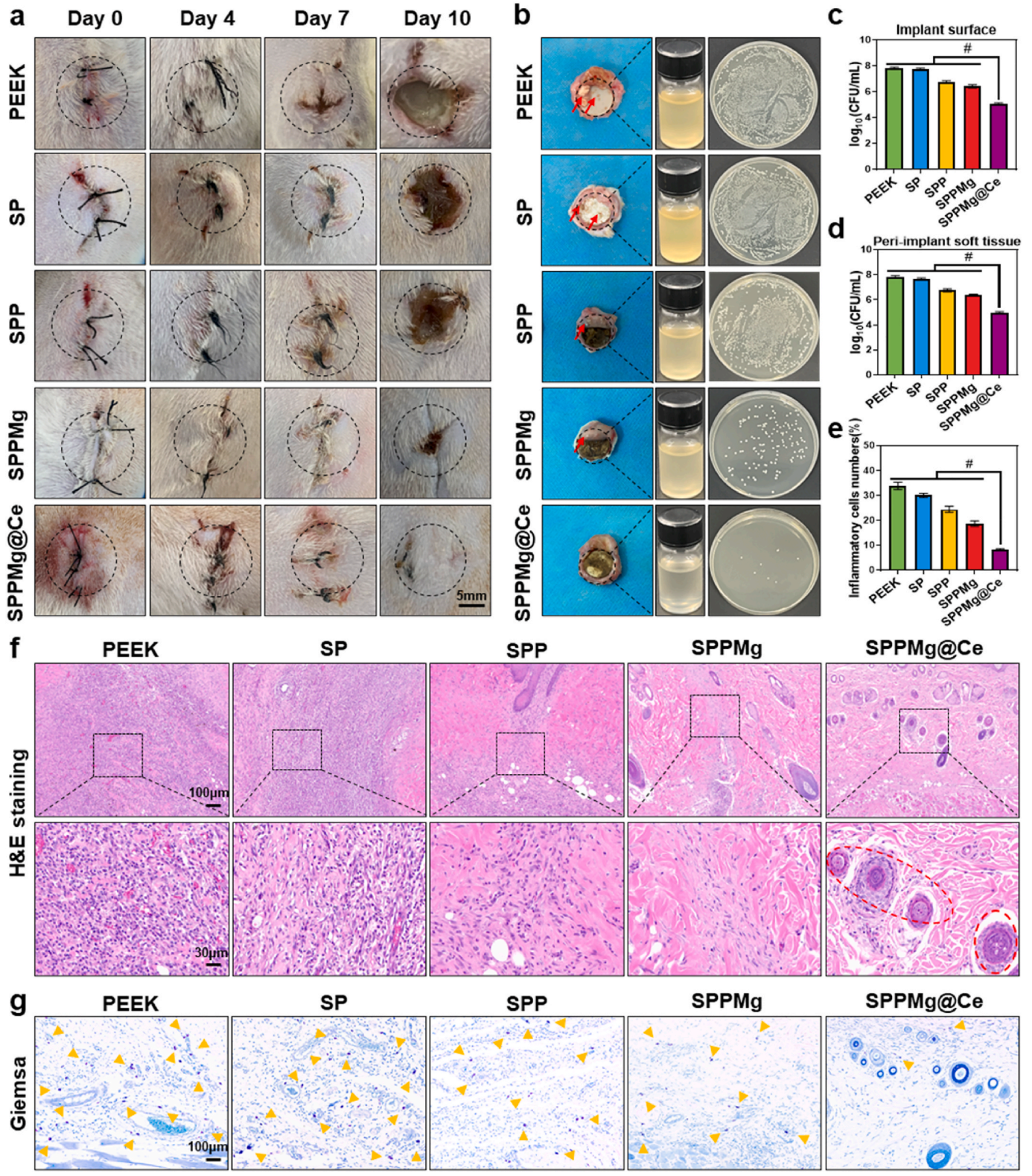

Fig. 6. ***In vivo*** **assessment of antibacterial activity in a rat subcutaneous infection model.** a) Photos of the skin tissue after five different treatments. Scale bar: 5 mm. b) Photographs of implant surfaces with peri-implant soft tissues (left), media cultured with various implants (middle), and bacterial colonies in various groups (right). c, d) Quantitative measurements of residual bacteria on implant surfaces and residual bacteria in peripheral tissues. e, f) H&E staining of the peri-implant soft tissues and quantification of inflammatory cells. Red circles in the SPPMg@Ce group indicate areas of normal follicle formation. Scale bars: 100 μm and 30 μm. g) Giemsa staining of the peri-implant soft tissues. Yellow arrows indicate the residual bacteria. Scale bar: 100 μm. n = 5 biologically independent experiments, and statistical analysis was obtained leveraging one-way ANOVA. Data are expressed as mean ± SD, *$p < 0.05$ and $^{\#}p < 0.001$.

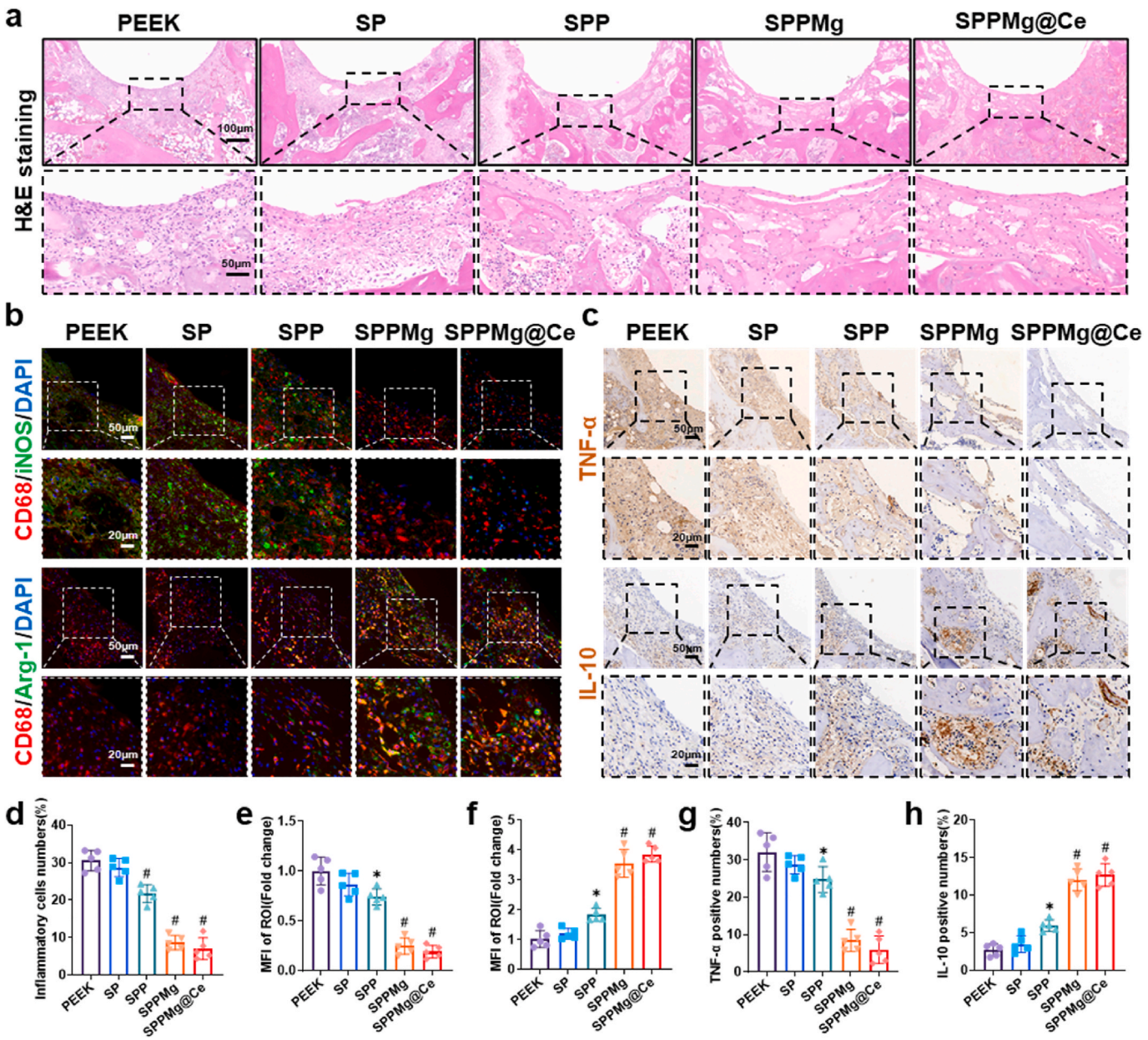

Fig. 7. Modified PEEK modulated macrophage polarization *in vivo*. a) Representative H&E staining images of the peri-implant tissue. Scale bars: 100 μm and 50 μm. b) Representative coimmunostaining photographs of the peri-implant tissue: green (M1 marker, iNOS and M2 marker, Arg-1), red (CD68, rat macrophage-specific antigen marker), and blue (nuclei). Scale bars: 50 μm and 20 μm. c) Representative immunohistochemical photographs of TNF-α and IL-10 in the peri-implant tissue. Scale bars: 50 μm and 20 μm. d) The quantitative result of infiltrating inflammatory cells. e, f) Quantitative coimmunostaining of double-positive macrophages. g, h) The quantitative result of TNF-α and IL-10 positive cells. n = 5 biologically independent experiments, and statistical analysis was obtained leveraging one-way ANOVA. Data are expressed as mean ± SD, *p < 0.05 and #p < 0.001.

respectively. In contrast, massive amounts of fresh bone tissue emerged in the SPPMg and SPPMg@Ce groups (Fig. 8a). Quantitative analysis of related bone parameters, including bone mineral density (BMD), bone volume per total tissue volume (BV/TV), bone surface per bone volume (BS/BV), trabecular number (Tb. N), and trabecular thickness (Tb. Th), further confirmed these results (Fig. 8b). Specifically, the bone tissues in the SPPMg and SPPMg@Ce groups exhibited extraordinarily higher BMD and BV/TV, presenting the optimal trabecular structural characteristics of the neo-bone under the same volume of interest (VOI), indicating that Mg^{2+}-modified biomaterials were more conducive than others to peri-implant osteoanagenesis. This evidence suggested that SPPMg and SPPMg@Ce demonstrated superior interfacial osteogenesis, likely attributed to the contribution of immunoactive Mg^{2+}. Robust connection between the implant and peripheral bone tissue is fundamental to ensure the reliability and longevity of biomaterials in clinical applications, so the push-out experiment was employed to detect the osseointegration effect of PEEK rods. As shown in Fig. S20, Supporting Information, the maximum push-out forces of the modified PEEK groups were all significantly higher than that of the PEEK group. Precisely, the SPPMg group and the SPPMg@Ce group demonstrated the highest maximum push-out forces and presented outstanding mechanical stability, further confirming that the Mg^{2+}-modified coatings can significantly boost the interfacial osteogenesis and augment the *in vivo* osseointegration.

To further explore the application potential of our modification strategy, H&E staining was performed and demonstrated a significant enhancement in new bone formation surrounding the SPPMg and SPPMg@Ce rods, with minimal inflammatory cell infiltration (Fig. 8c).

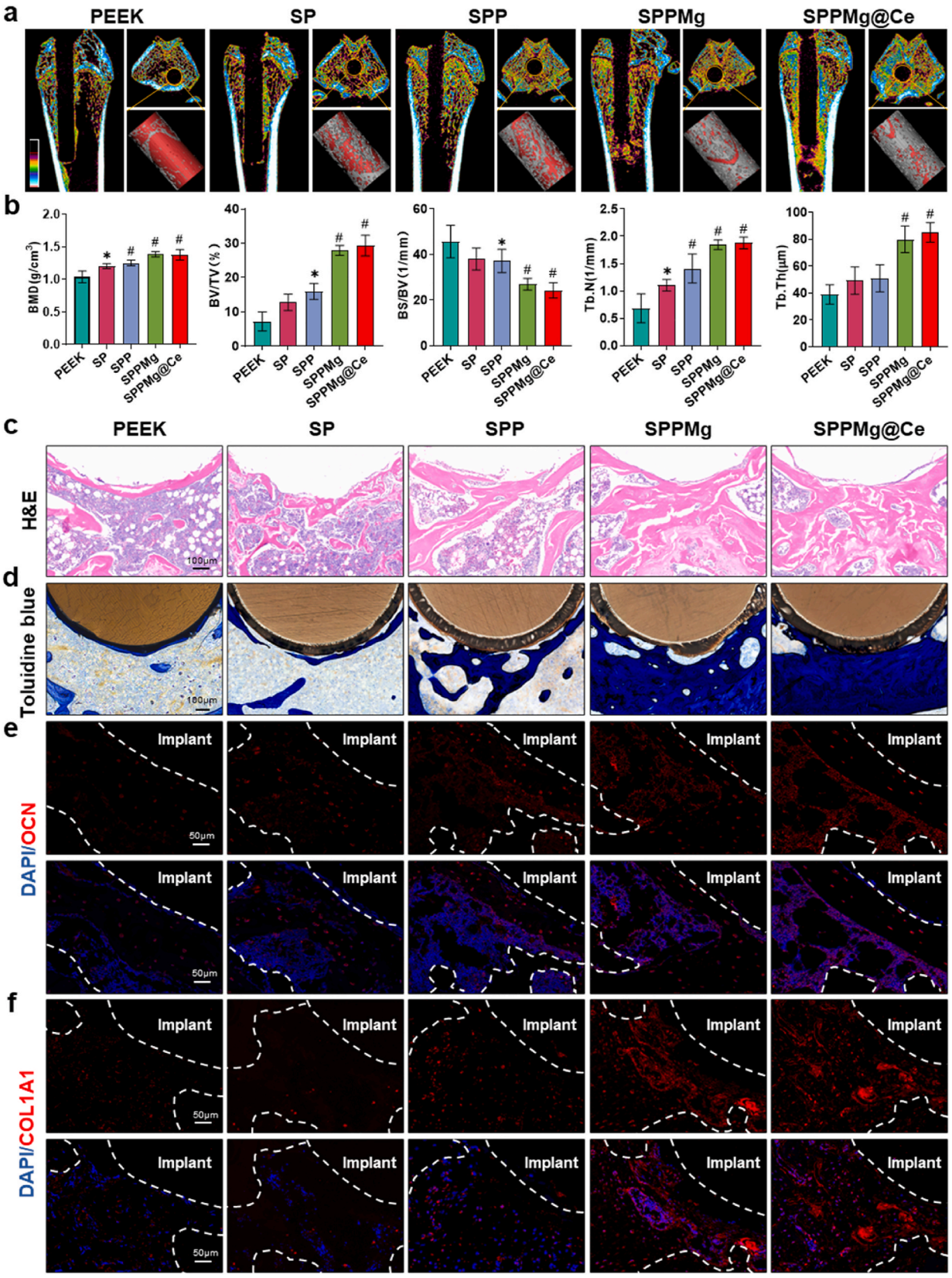

Fig. 8. Mg^{2+}-modified PEEK modulated surface bone remodeling *in vivo*. a) Micro-CT 3D photographs of femurs containing PEEK, SP, SPP, SPPMg and SPPMg@Ce implants. Cancellous bone features yellow markings, cortical bone features blue markings, and the medullary cavity is shown in black when aligned with the colorful ruler at the bottom left. b) Quantitative assessment of bone production around implants based on BMD, BV/TV, BS/BV, Tb. N, and Tb. Th. c) H&E staining photographs of the peri-implant tissue. Scale bar: 100 μm. d) Toluidine blue staining photographs of the peri-implant tissue. Scale bar: 100 μm. e, f) Immunofluorescence staining of osteogenesis-associated markers in peri-implant tissue (red: OCN and COLA1; blue: DAPI). Scale bar: 50 μm. n = 5 biologically independent experiments, and statistical analysis was obtained leveraging one-way ANOVA. Data are expressed as mean ± SD, *$p < 0.05$ and $^{\#}p < 0.001$.

Subsequent toluidine blue staining of hard-tissue sections revealed more neonatal bones and higher circumferential contact ratios in the SPPMg and SPPMg@Ce groups (Fig. 8d and Fig. S21a, Supporting Information). Sequential immunofluorescence labeling was further performed to probe into the expression of osteoblast marker proteins *in vivo*, and similar results were obtained. In the PEEK group, the osteogenesis-related proteins OCN and COL1A1 were only expressed in a small portion of the bone tissues around the implants. In contrast, the SPPMg and SPPMg@Ce groups showed higher levels of positive fluorescence signals for these proteins (Fig. 8e, f and Figs. S21b and c, Supporting Information), suggesting their role in promoting interfacial osteogenesis and enhancing osseointegration *in vivo*. Major organs, such as the heart, liver, spleen, lung, and kidney, were tested through H&E staining to determine the toxicity of the implants *in vivo*, and intact tissue microstructures were detected, demonstrating the cytocompatibility of our approach (Fig. S22, Supporting Information). Conventional bone repair materials typically prioritized optimizing osteogenesis and often employed inert materials to prevent immune rejection. Here, we presented a novel PEEK biomaterial that displayed phenomenal immunomodulatory functions and direct osteoinductive properties, along with an eximious safety profile, ameliorating the osseointegration of implants.

In this study, PDA was employed as a "bridge" to construct biomimetic coatings containing metal ions, which is a simple and easy-to-apply surface modification method that can occur under mild reaction conditions [47]. Electrostatic spinning is favorable for efficient, precise and adjustable drug loading, which further facilitates cost-effective large-scale manufacturing [67]. However, further enhancement of the homogeneity and stability of the coating, and controllability of the deep drug release may become potential challenges for scaling up the modified materials to commercial scale production. Given the remarkable processability of the electrospun nanofibers [67,68], it may be feasible to optimize from this point on prospectively. In addition, there are some other limitations of this study, such as the lack of more in-depth delving regarding the antimicrobial mechanism. More systematic and comprehensive work will be conducted in the future to provide additional alternatives for the development of tissue regeneration biomaterials.

3. Conclusion

In summary, we successfully synthesized a microenvironment responsive PEEK biomaterial implant with antibacterial, immunomodulatory and osteoinductive properties through a PDA-based chelation reaction and SF-based electrospinning. This approach offers a straightforward method for co-modifying PEEK implants with immunoactive metal ions (e.g., Mg^{2+}) and antibacterial nanoparticles (e.g., CNPs). The pH-responsiveness of SF allows for the on-demand release of CNPs, preventing premature and excessive metallic element leakage and eradicating bacteria by destroying the bacterial membrane. Subsequently, the sustained release of Mg^{2+}, which is coordinated with catechol residues, fosters a favorable osteoimmune microenvironment by facilitating macrophage subphenotype shift from M1 to M2 to suppress the expression of inflammatory cytokines and enhance the osteogenic differentiation of BMSCs, ultimately ameliorating osseointegration surrounding the bone implant *in vivo*. Therefore, our proposed strategy, which integrates bactericidal properties and macrophage-associated osteoimmunomodulation based on pH responsiveness and the sustained release of metal ions, may offer an alternative approach to combat refractory implant-related infections and address issues of substandard osseointegration.

4. Materials and methods

4.1. Isolation of SF and characterization of CNPs

The SF was acquired in the manner described previously [69]. In particular, silkworm cocoons were sliced into tiny fragments and submerged in a water-based solution containing 0.02 M Na_2CO_3 for 30 min. Next, the cocoons were purged using deionized water. SF was dissolved in a LiBr solution (9.3 M) at 60 °C for 4 h. Next, the remedy was permeated against deionized water utilising dialysis bags while blending for 48 h. Later on, the compound was centrifuged to eliminate any impurities. To acquire the SF sponge, the remaining SF solution was subjected to freeze-drying at a temperature of −55 °C and a pressure of 0.07 mb for 72 h. CNPs were purchased from Sigma-Aldrich (USA). The purity of the CNPs was greater than 99.9 %. The structure and particle size distribution were observed by TEM (FEI Talos F200X G2, USA).

4.2. Surface functionalization of PEEK

The PEEK materials were separated into two distinct forms: a circular material measuring 1 mm × 14 mm × 14 mm and a cylindrical material with a length of 8 mm and a diameter of 2 mm. Initially, the PEEK was submerged in a solution of sulfuric acid (98 wt %) while being stirred magnetically for a duration of 3 min. This was then followed by subjecting them to a hydrothermal process at 100 °C for a period of 6 h, in order to eliminate any remaining sulfuric acid (labeled SP). Following this, the SP materials were submerged in a reaction mixture with a pH of 8.5, comprising a 10 mM Tris-HCl buffer solution and 2 mM dopamine for 24 h (labeled SPP). In addition, a set of SPP materials were also immersed in a reaction mixture of 10 mM Tris and 50 mg/mL $MgCl_2$ at pH 8.5. Under the same conditions as described in the previous step, this immersion also continued for 24 h. Subsequently, all the specimens were meticulously scrubbed three times with distilled water for a duration of 5 min each (labeled SPPMg). In addition, the CNPs were dissolved in a solution of HFIP and then homogenized via sonication (Bransonic Sonicator 210) in an ultrasonic bath for 30 min at a frequency of 20 kHz. The SF sponge was dissolved in a solution containing CNPs and churned overnight with electromagnetic stirring. Before electrospinning, the blended mixture was subjected to sonication for 30 min. The homogenized solution was then spun three times over the SPPMg materials, which were subsequently coated with three layers of filaments (labeled SPPMg@Ce).

4.3. Surface characterization

The PEEK, SP, SPP, SPPMg and SPPMg@Ce were evaluated for surface morphology with SEM (Sirion 200, FEI, USA) and AFM (Dimension ICON, Bruker, USA). The chemical compositions of the various PEEK specimens were analyzed utilising XPS (AXIS Ultra DLD, Japan) and EDS (Sirion 200, FEI). To assess the surface wetness of PEEK, SP, SPP, SPPMg and SPPMg@Ce, a contact angle instrument called Theta Lite (Biolin Scientific in Finland) was utilized.

4.4. Release of CNPs and Mg^{2+}

In order to investigate the release of CNPs and Mg^{2+}, the specimens (SPPMg and SPPMg@Ce) (n = 3) were dipped into PBS at diverse pH values (pH = 5.0, 6.0, and 7.4) for 28 days. The whole solution was gathered and replenished with fresh PBS at scheduled times (1 day, 2 days, 5 days, 7 days, 10 days, 14 days, 21 days, and 28 days). The release behavior of the CNPs and Mg^{2+} was then detected utilising an inductively coupled plasma-optical emission spectrometer (ICP–OES, Thermo Fisher iCAP PRO, USA).

4.5. In vitro antibacterial activity

The antimicrobial agents used were *E. coli* (ATCC 25922) and *S. aureus* (ATCC 25923). All the bacterial strains were cultivated in Luria–Bertani (LB) medium (Sigma–Aldrich, USA). SEM was utilized to investigate the bacterial topography. Briefly, 500 μL bacterial suspension was inoculated onto PEEK, SP, SPP, SPPMg and SPPMg@Ce for 24 h

at 37 °C. After 3 gentle washes with PBS, bacteria adhering to different specimens were immobilised with glutaraldehyde (4 wt%) for 24 h and then dehydrated with graded ethanol. After vacuum drying, the PEEK substrates were sputter plated with gold, and the topography of the adhering bacteria was subsequently investigated via SEM. Furthermore, the biofilms on PEEK, SP, SPP, SPPMg and SPPMg@Ce were evaluated via a crystal violet assay. In brief, PBS was used to wash the different PEEK samples after the medium and loose bacteria were removed. Crystal violet staining solution was then used to color the samples after they had been grown in anhydrous ethanol. The biofilm was solubilised in 30 % glacial acetic acid after the excess dye solution was removed, which took half an hour. Finally, the solutions were analyzed after enzyme labeling, and a spectrophotometric microplate reader was utilized to detect the absorbance at 590 nm (Bio-Rad 680, USA). Confocal laser scanning microscopy (CLSM, LSM 710, Germany) was utilized to examine the 3D structure of the biofilms.

To measure the antimicrobial activities of PEEK, SP, SPP, SPPMg and SPPMg@Ce, we quantified the quantity of surviving bacteria using the spreading plate method (SPM). Specifically, specimens were plated in 24-well plates with 500 μL of bacterial suspension in LB media at various pH levels (7.4 and 5.0) for 24 h at 37 °C. Following incubation, supersonic elution was performed with sterile PBS containing 0.1 % Tween 80 to separate the cultured bacteria of each group from the sample surface, after which the sample surface was rinsed with sterile PBS. Sterile PBS was used to dilute the bacterial eluent from the various groups to the desired concentration. Following this step, 100 μL of diluted bacterial eluate was applied to LB agar plates and nurtured at 37 °C for 24 h. Next, the amount of colony-forming units (CFU) was computed and photographed, and the survival rate of the bacteria was determined by the formula: Survival rate = B/A × 100 %. The mean count of bacterial colonies in the remaining experimental groups is shown in B, whereas the mean number of occurrences in the control group (PEEK samples) is represented in A. The membrane permeability of bacteria of various PEEK groups was estimated utilising the ONPG assay (Sigma-Aldrich, USA). Normally, 500 μL of bacterial suspension (1×10^6 CFU/mL) was incubated on PEEK, SP, SPP, SPPMg and SPPMg@Ce for 6 h. After that, the attached bacteria were exposed to 500 μL of ONPG solution (0.75 M, NaH_2PO_4 buffer solution) for a duration of 2 h. A spectrophotometric microplate reader was then utilized to determine the absorbance of the resulting yellow supernatant at a wavelength of 405 nm. The amount of protein leakage was measured utilising a BCA protein assay kit (Thermo Scientific, USA) depending on the manufacturer's specifications.

4.6. Cell culture

RAW264.7 cells were acquired from the Shanghai Cell Bank of the Chinese Academy of Sciences. RAW264.7 cells were cultivated in high-glucose Dulbecco's modified Eagle's medium (DMEM, HyClone) supplemented with 10 % fetal bovine serum (FBS, Gibco) and cultivated at 37 °C in a 5 % CO_2 environment. The medium for cultivating cells was replaced every 48 h.

Bone marrow mesenchymal stem cells (BMSCs) derived from the bone marrow of male Sprague–Dawley rats aged 6 weeks were isolated. In brief, femurs and tibiae were gained and isolated from muscle and connected tissue. Following the removal of the bone ends, the bone marrow suspension was rinsed and suspended in α-MEM (Gibco) with the addition of 10 % FBS and 1 % penicillin/streptomycin (PS, Gibco). The cell suspensions were filtered through a 70 μm filter (Millipore, Ireland). The cells were cultured at 37 °C in 5 % CO_2, and the medium for cultivating the cells was replaced every 48 h. When the cells reached 80–90 % confluence, the cells were separated from the culture dish. Pure BMSCs were gradually acquired by replacing the medium with fresh medium.

4.7. Cytocompatibility

RAW264.7 cells and BMSCs were inoculated onto samples treated with various PEEK surfaces for 24 h and purified 3 times using sterile PBS. Cell viability was evaluated utilising a live/dead cell staining kit (Yeasen, China). Utilising a fluorescence microscope, fluorescence pictures were captured (Axio Imager M1, Zeiss, Germany). The cytotoxicity of various PEEK samples on cell proliferation was measured utilising a cell counting kit-8 (CCK-8, Yessen, China) assay. To explore the adhesion and dispersion of BMSCs on the diverse PEEK materials, FITC-labeled phalloidin staining (Yeasen, China) was performed in this work. Then, 4 % paraformaldehyde was used to fix the samples. After 24 h of incubation, the cells got permeated with 0.1 % (v/v) Triton X-100, blocked with 4 % bovine serum albumin (BSA), and stained with FITC-labeled phalloidin (Yeasen, China) and 4′,6-diamidino-2-phenylindole hydrochloride (DAPI, Beyotime, China). Fluorescence microscopy was utilized to observe the cell nuclei and cytoskeletal actin.

4.8. Macrophage polarization in vitro

RAW 264.7 cells were used in experiments to validate the control of macrophage polarization after Mg^{2+} alteration. After being seeded onto different specimens, RAW 264.7 cells were driven to produce the M1 phenotype utilising lipopolysaccharide (LPS, 100 ng/mL) for 24 h. The procedure for immunofluorescence staining was followed as previously stated after 48 h culturing. Primary antibodies (iNOS, 1:200, Abcam; Arg-1, 1:200, Abcam) were used after blocking, and the cells were cultured for 12 h at 4 °C. Then, the cells were cultured with IgG H&L (Alexa Fluor 488; Abcam) and DAPI solution. Flow cytometry was conducted by seeding cells in 6-well plates at a concentration of 5×10^5 cells/well. After being nurtured with intervention for 48 h, the cells were harvested, subjected to nonspecific protein blocking, and the cell membranes were disrupted. Next, the cells were treated with antibodies against CD11b, CD206 or CD86 (BD Pharmingen, USA) at 4 °C for 30 min. Lastly, the cells were suspended again and evaluated utilising a FACS Caliber flow cytometer (BD, Franklin Lakes, NJ, USA). CellQuest (BD) and Flow JOV10 (BD) were utilized for data processing in order to examine the various groups. To assess the expression levels of *Tnfa*, *Il1b*, *Il10*, and *Bmp-2* using RT−qPCR, total RNA was collected after 24 h culturing. The primer sequences for these genes are included in Table S1, Supporting Information. RAW 264.7 cells were obtained after 24 h of culture for RNA-seq analysis from the control group (cells cultured on bare PEEK plates) and SPPMg@Ce group (cells cultured on SPPMg@Ce plates). Specifically, total RNA was isolated using the TRIzol reagent, following the manufacturer's guidelines. The purity and concentration of the RNA were determined with a NanoDrop 2000 spectrophotometer (Thermo Scientific, USA), while RNA integrity was evaluated using an Agilent 2100 Bioanalyzer (Agilent Technologies, Santa Clara, CA, USA). Subsequently, libraries were prepared using the TruSeq Stranded mRNA LT Sample Prep Kit (Illumina, San Diego, CA, USA), adhering to the provided instructions. Sequencing was performed on an Illumina HiSeq X Ten platform, yielding 150 bp paired-end reads. The transcriptome sequencing was carried out by OE Biotech Co., Ltd. (Shanghai, China). Genes exhibiting a p-value ≤ 0.05 and a fold-change ≥ 2 between samples were considered differentially expressed.

4.9. Osteogenic differentiation in vitro

To investigate the potential impact of SPPMg and SPPMg@Ce materials on BMSCs development via macrophage polarization regulation, we gathered supernatants from RAW264.7 cells nurtured on different PEEK surfaces while experiencing inflammation. Afterwards, the liquid above was spun at a speed of × 60 g for 5 min to eliminate any remaining cells. The solution was then stored at a temperature of −80 °C until it was needed for future use. Additionally, the liquid above was filtered through a 0.22 μm filter (Millipore, Ireland) and combined with α-MEM

at a ratio of 1:2 to obtain CM. BMSCs were placed in 24-well plates at a concentration of 2×10^4 cells per well in α-MEM for 12 h, after which CM containing osteogenic elements (0.1 μM dexamethasone, 10 mM β-glycerophosphate and 0.25 mM ascorbate) was added to the medium for future culture. The cells were immobilised with 4 % paraformaldehyde fixative solution after culturing for 14 and 21 days. Then, for ALP and ARS staining, BCIP/NBT working solution and alizarin red S (ARS) staining solution (Beyotime, China) were used. An alkaline phosphatase detection kit (Beyotime) was employed to measure ALP activity, and perchloric acid was used to dissolve ARS for semi-quantitative analysis. RT−qPCR was carried out to determine the expression of osteogenesis-associated genes (e.g., *Alp*, *Col1a1*, *Runx2*, and *Opn*) in the treated BMSCs after acquiring total RNA. Table S1, Supporting Information lists the primer sequences for these genes. Immunofluorescence staining was operated to measure the expression of osteogenesis-associated proteins. In brief, BMSCs were treated with 4 % paraformaldehyde and made permeable using 0.2 % Triton-X 100 (Beyotime). Afterwards, the cells were blocked with immunostaining blocking solution before they were nurtured with primary antibodies (Runx2, 1:200, Abcam). Next, the BMSCs were incubated with the corresponding secondary antibodies, phalloidin and DAPI. In the end, the fluorescence microscope was carried out to detect the cells. The cells were nurtured on various surfaces with α-MEM including osteogenic components to evaluate the direct impact of SPPMg and SPPMg@Ce on BMSCs development. The abovementioned methods for detecting osteogenic differentiation (e.g., ALP staining, ARS staining, RT−qPCR and immunofluorescence staining) were implemented to detect direct osteogenic activity.

4.10. Animal models

The Ethics Committee of Soochow University approved all the experiments (ethics approval number: SUDA20230428A01), which were performed in compliance with the Guidelines for the Care and Use of Laboratory Animals. Male Sprague−Dawley rats, aged 6–8 weeks, were randomised into five groups: PEEK, SP, SPP, SPPMg, and SPPMg@Ce. The surgical site was chosen to be the flat lateral aspect of the femoral condyle. After proper anesthesia and strict sterilization, a hole was drilled at the midpoint of the femoral condyle. Subsequently, a PEEK rod (8 mm long, 2 mm in diameter) was vertically transplanted into the distal femur. Afterwards, the cuts were stitched in multiple layers, and all the animals obtained intramuscular antibiotics for 3 days following the procedure. The animals were euthanized at 2 and 8 weeks following the surgical operation to conduct the immunomodulatory test and osteogenic test, respectively. To investigate the efficacy of various treatments for deep wound infections *in vivo*, we employed a rat model of subcutaneous infection, which closely mimics human implant-associated infections. Before the procedure, the rats were sedated with pentobarbital injected into their abdomens. Next, the skin on their backs was shaved, and a 1.4-cm cut was established. After a premade PEEK substance (1 mm × 14 mm × 14 mm) was inserted under the skin, the incision was meticulously sealed. Finally, 100 μl (1 x10^7 CFU/ml) of *S. aureus* was injected into the surface of the samples by means of a microsyringe to minimize leakage of the bacterial suspension. On day 10, the rats were sacrificed, and the subcutaneous implant and the soft tissue surrounding the implant were aseptically collected.

4.11. Micro-CT evaluation and the push-out experiment

After being removed from the muscle tissue, femurs containing the implant material were fixed in neutral formalin for 12 h. A micro-CT system (SkyScan1172, Belgium) was employed to scan the collected bones. The parameters for operating the equipment were configured as follows: voltage 50 kV, current 500 μA, scanning layer thickness 18 μm, scanning range 2 cm × 2 cm, rotation step of 0.15°, and 1 mm Al filter optimizing the contrast. Next, we reconstructed 3D images and evaluated bone tissue-related parameters. During this procedure, we analyzed bone parameters, including bone mineral density (BMD), bone surface per bone volume (BS/BV), bone volume per total tissue volume (BV/TV), trabecular number (Tb. N) and trabecular thickness (Tb. Th), by choosing the area around the implants as the region of interest (ROI) via CTAn software. With Mimics Software, 3D reconstructed images were produced (Version 21.0, Materialise, Belgium). The push-out force testing experiment was conducted to assess the maximum load of various PEEK rods. After the femurs containing the PEEK rods were anchored in place with the dental cement, the PEEK rods were slowly pushed using a material testing system (HY1080, China) until they were completely pushed out. The maximum push-out force was detected and recorded.

4.12. Histological, immunohistochemical and immunofluorescence staining

Harvested skin tissues were fixed with paraformaldehyde (4 %) after washing with 0.9 % NaCl solution and dehydrated. Next, the skin tissues were paraffin-embedded to obtain histological sections. The microstructure of the skin tissue was estimated using H&E staining in response to the invasion of inflammatory cells. Giemsa staining was utilized to differentiate between bacteria and cells when observing an infection.

All harvested femurs were fixed in 10 % formalin for 2 days. A portion of the collected femurs was sectioned in the absence of decalcification. For a period of 4–5 weeks, the remaining femurs were treated with 10 % ethylenediaminetetraacetic acid (EDTA, Sigma−Aldrich) for decalcification. After removing the PEEK rods, the specimens were then meticulously embedded and sliced into sections. H&E staining was employed to detect microstructural variations in the specimen tissues. Sections were characterized by CLSM. Osseointegration under undecalcified conditions was assessed by toluidine blue staining, and the bone-implant contact parameters (BIC) were evaluated.

The expression of TNF-α and IL-10 were determined employing immunohistochemistry (IHC). Briefly, tissue sections were deparaffinized and gradient hydrated, and primary antibodies, which included TNF-α and IL-10 (Servicebio, China), were subsequently added and nurtured at 4 °C overnight. The sections were then nurtured with the corresponding secondary antibody for 30 min. Chromogenic reactions were induced with a DAB kit (Beyotime, China). Random areas were picked from the whole field of vision.

Immunofluorescence staining was employed to evaluate variations in macrophage polarization and osteogenic indices. Paraffin-embedded tissue slices were baked and then rehydrated. Tissue antigen retrieval and blocking were subsequently conducted. Primary antibodies against iNOS, Arg-1, CD68, OCN and COL1A1 (Servicebio, China) were added and nurtured with the sections at 4 °C overnight. The appropriate fluorescent secondary antibody was chosen for each sample and incubated at room temperature for 1 h. After incubation with DAPI, the sections were sealed using an antifluorescence quenching mounter and evaluated with a laser confocal fluorescence microscope. ImageJ software was utilized to measure the fluorescence intensity.

4.13. Statistical analysis

The values are presented as the mean ± standard deviation (SD). Student's t-test was employed to evaluate the significance of differences between two groups. One-way ANOVA was leveraged to compare the data between multiple groups. GraphPad Prism 8 (GraphPad Software, CA, USA) was employed for statistical analysis. Significance is shown as $^{*}p < 0.05$, $^{\#}p < 0.001$.

Data availability

The data that support the findings of this study are available from the corresponding authors upon reasonable request.

Ethics approval and consent to participate

The content of experimental animal research and animal ethics involved in this project has been reviewed by the Ethics Committee of Soochow University, and is in line with the GB/T35892-2018 Ethical Review Standard for Experimental Animal Welfare and the Implementing Rules for the Management of Medical Experimental Animals issued by the Ministry of Health, as well as the Statutes and Review Methods of the Ethics Committee of Soochow University, which meet the requirements for animal ethics. The constitution and review method of the Ethics Committee of Soochow University meet the requirements of animal ethics and are approved for implementation. **SUDA20230428A01**.

CRediT authorship contribution statement

Miao Chen: Writing – original draft, Software, Methodology, Data curation, Conceptualization. **Yusen Qiao:** Visualization, Software, Methodology, Data curation. **Lei Yu:** Software, Methodology, Data curation. **Wei Wang:** Methodology, Data curation. **Wentao Wang:** Software, Methodology. **Haifu Sun:** Software. **Yaozeng Xu:** Resources, Funding acquisition. **Jiaxiang Bai:** Writing – review & editing, Supervision, Conceptualization. **Jun Zhou:** Writing – review & editing, Resources, Funding acquisition, Conceptualization. **Dechun Geng:** Writing – review & editing, Supervision, Resources, Funding acquisition, Conceptualization.

Declaration of competing interest

The authors declare that they have no known competing financial interests or personal relationships that could have appeared to influence the work reported in this paper.

Acknowledgements

This work was supported by the China National Postdoctoral Program for Innovative Talents (BX20230350), the National Natural Science Foundation of China (82472525, 82402780, 82002321, 82072425, and 82072498), the China Postdoctoral Science Foundation (2024M753130), the Natural Science Foundation of Jiangsu Province (BK2021650), the Jiangsu Medical Research Project (ZD2022014), the Special Project of Diagnosis and Treatment Technology for Key Clinical Diseases in Suzhou (LCZX202003 and LCZX202302), the Research Funds of Centre for Leading Medicine and Advanced Technologies of IHM (2023IHM02007), the Priority Academic Program Development of Jiangsu Higher Education Institutions (PAPD), the Suzhou Science and Technology Project (SKJY2021067), the Innovation Center Project of Orthopedic Surgery in Jiangsu Province (CXZX202209), the Foundation of National Center for Translational Medicine (Shanghai) SHU Branch (SUITM-202301, SUITM-202403).

Appendix A. Supplementary data

Supplementary data to this article can be found online at https://doi.org/10.1016/j.bioactmat.2024.09.017.

References

[1] M. Veletic, E.H. Apu, M. Simic, J. Bergsland, I. Balasingham, C.H. Contag, N. Ashammakhi, Implants with sensing capabilities, Chem Rev 122 (2022) 16329–16363.
[2] Y. Zhang, J. Cui, K.Y. Chen, S.H. Kuo, J. Sharma, R. Bhatta, Z. Liu, A. Ellis-Mohr, F. An, J. Li, Q. Chen, K.D. Foss, H. Wang, Y. Li, A.M. McCoy, G.W. Lau, Q. Cao, A smart coating with integrated physical antimicrobial and strain-mapping functionalities for orthopedic implants, Sci. Adv. 9 (2023) eadg7397.
[3] J. Hou, Z. Xiao, Z. Liu, H. Zhao, Y. Zhu, L. Guo, Z. Zhang, R.O. Ritchie, Y. Wei, X. Deng, An amorphous peri-implant ligament with combined osteointegration and energy-dissipation, Adv Mater 33 (2021) e2103727.
[4] H.D. Jung, T.S. Jang, L. Wang, H.E. Kim, Y.H. Koh, J. Song, Novel strategy for mechanically tunable and bioactive metal implants, Biomaterials 37 (2015) 49–61.
[5] Y. Zhang, Z. Cheng, Z. Liu, X. Shen, C. Cai, M. Li, Z. Luo, Functionally tailored metal-organic framework coatings for mediating Ti implant osseointegration, Adv. Sci. 10 (2023) e2303958.
[6] G. Chu, M. Guan, J. Jin, Y. Luo, Z. Luo, T. Shi, T. Liu, C. Zhang, Y. Wang, Mechanochemically reprogrammed interface orchestrates neutrophil bactericidal activity and apoptosis for preventing implant-associated infection, Adv Mater (2024) e2311855.
[7] M. Alizadeh-Osgouei, Y. Li, C. Wen, A comprehensive review of biodegradable synthetic polymer-ceramic composites and their manufacture for biomedical applications, Bioact. Mater. 4 (2019) 22–36.
[8] N. Li, J. Bai, W. Wang, X. Liang, W. Zhang, W. Li, L. Lu, L. Xiao, Y. Xu, Z. Wang, C. Zhu, J. Zhou, D. Geng, Facile and versatile surface functional polyetheretherketone with enhanced bacteriostasis and osseointegrative capability for implant application, ACS Appl. Mater. Interfaces 13 (2021) 59731–59746.
[9] S. He, C. Duan, S. Wang, Y. Yu, Y. Kei Chan, X. Shi, J. Huang, S. Wang, S. Peng, Y. Deng, Fusion peptide-engineered polyetheretherketone implants with photo-assisted anti-pathogen and enhanced angiogenesis for in vivo osseointegrative fixation, Chem. Eng. J. 446 (2022).
[10] W. Yin, M. Chen, J. Bai, Y. Xu, M. Wang, D. Geng, G. Pan, Recent advances in orthopedic polyetheretherketone biomaterials: material fabrication and biofunction establishment, Smart Materials in Medicine 3 (2022) 20–36.
[11] X.S. Gao, H.H. Wang, S.F. Luan, G.Y. Zhou, Synthesis and 3D-printing of isosorbide-based poly(aryletherketone) for carbon neutral manufacturing, Chem. Eng. J. 477 (2023).
[12] S.M. Kurtz, J.N. Devine, PEEK biomaterials in trauma, orthopedic, and spinal implants, Biomaterials 28 (2007) 4845–4869.
[13] W. Liu, J. Li, M. Cheng, Q. Wang, Y. Qian, K.W.K. Yeung, P.K. Chu, X. Zhang, A surface-engineered polyetheretherketone biomaterial implant with direct and immunoregulatory antibacterial activity against methicillin-resistant Staphylococcus aureus, Biomaterials 208 (2019) 8–20.
[14] L. Ouyang, Y. Zhao, G. Jin, T. Lu, J. Li, Y. Qiao, C. Ning, X. Zhang, P.K. Chu, X. Liu, Influence of sulfur content on bone formation and antibacterial ability of sulfonated PEEK, Biomaterials 83 (2016) 115–126.
[15] M. Li, J. Bai, H. Tao, L. Hao, W. Yin, X. Ren, A. Gao, N. Li, M. Wang, S. Fang, Y. Xu, L. Chen, H. Yang, H. Wang, G. Pan, D. Geng, Rational integration of defense and repair synergy on PEEK osteoimplants via biomimetic peptide clicking strategy, Bioact. Mater. 8 (2022) 309–324.
[16] T. Wang, J. Bai, M. Lu, C. Huang, D. Geng, G. Chen, L. Wang, J. Qi, W. Cui, L. Deng, Engineering immunomodulatory and osteoinductive implant surfaces via mussel adhesion-mediated ion coordination and molecular clicking, Nat. Commun. 13 (2022) 160.
[17] C.M. Li, C.C. Guo, V. Fitzpatrick, A. Ibrahim, M.J. Zwierstra, P. Hanna, A. Lechtig, A. Nazarian, S.J. Lin, D.L. Kaplan, Design of biodegradable, implantable devices towards clinical translation, Nat. Rev. Mater. 5 (2020) 61–81.
[18] S. Liu, W. Liu, Q. Yang, S. Yang, Y. Yang, L. Fan, Y. Zhang, B. Qi, Z. Shi, X. Wei, L. Zhu, T. Li, Non-coding-RNA-activated core/chitosan shell nanounits coated with polyetheretherketone for promoting bone regeneration and osseointegration via osteoimmunology, ACS Appl. Mater. Interfaces 15 (2023) 12653–12668.
[19] H. Kang, S. Kim, D.S.H. Wong, H.J. Jung, S. Lin, K. Zou, R. Li, G. Li, V.P. Dravid, L. Bian, Remote manipulation of ligand nano-oscillations regulates adhesion and polarization of macrophages in vivo, Nano Lett. 17 (2017) 6415–6427.
[20] J. Bai, H. Wang, H. Chen, G. Ge, M. Wang, A. Gao, L. Tong, Y. Xu, H. Yang, G. Pan, P.K. Chu, D. Geng, Biomimetic osteogenic peptide with mussel adhesion and osteoimmunomodulatory functions to ameliorate interfacial osseointegration under chronic inflammation, Biomaterials 255 (2020) 120197.
[21] R.J. Miron, D.D. Bosshardt, OsteoMacs: key players around bone biomaterials, Biomaterials 82 (2016) 1–19.
[22] P.J. Murray, Macrophage polarization, Annu. Rev. Physiol. 79 (2017) 541–566.
[23] M.U. Joshi, S.P. Kulkarni, M. Choppadandi, M. Keerthana, G. Kapusetti, Current state of art smart coatings for orthopedic implants: a comprehensive review, Smart Materials in Medicine 4 (2023) 661–679.
[24] Y. Zhu, H. Liang, X. Liu, J. Wu, C. Yang, T.M. Wong, K.Y.H. Kwan, K.M.C. Cheung, S. Wu, K.W.K. Yeung, Regulation of macrophage polarization through surface topography design to facilitate implant-to-bone osteointegration, Sci. Adv. 7 (2021).
[25] J. Li, X. Jiang, H. Li, M. Gelinsky, Z. Gu, Tailoring materials for modulation of macrophage fate, Adv Mater 33 (2021) e2004172.
[26] T. Liu, L. Wang, P. Liang, X. Wang, Y. Liu, J. Cai, Y. She, D. Wang, Z. Wang, Z. Guo, S. Bates, X. Xia, J. Huang, J. Cui, USP19 suppresses inflammation and promotes M2-like macrophage polarization by manipulating NLRP3 function via autophagy, Cell. Mol. Immunol. 18 (2021) 2431–2442.
[27] G. Lu, Y. Xu, Q. Liu, M. Chen, H. Sun, P. Wang, X. Li, Y. Wang, X. Li, X. Hui, E. Luo, J. Liu, Q. Jiang, J. Liang, Y. Fan, Y. Sun, X. Zhang, An instantly fixable and self-adaptive scaffold for skull regeneration by autologous stem cell recruitment and angiogenesis, Nat. Commun. 13 (2022) 2499.
[28] Z.J. Lin, D.N. Shen, W.X. Zhou, Y.F. Zheng, T.T. Kong, X.Y. Liu, S.L. Wu, P.K. Chu, Y. Zhao, J. Wu, K.M.C. Cheung, K.W.K. Yeung, Regulation of extracellular bioactive cations in bone tissue microenvironment induces favorable osteoimmune conditions to accelerate bone regeneration, Bioact. Mater. 6 (2021) 2315–2330.
[29] L. Zheng, S. Zhao, Y. Li, J. Xu, W. Yan, B. Guo, J. Xu, L. Jiang, Y. Zhang, H. Wei, Q. Jiang, Engineered MgO nanoparticles for cartilage-bone synergistic therapy, Sci. Adv. 10 (2024) eadk6084.
[30] X. Qiao, J. Yang, Y. Shang, S. Deng, S. Yao, Z. Wang, Y. Guo, C. Peng, Magnesium-doped nanostructured titanium surface modulates macrophage-mediated

inflammatory response for ameliorative osseointegration, Int J Nanomedicine 15 (2020) 7185–7198.
[31] W. Qiao, K.H.M. Wong, J. Shen, W. Wang, J. Wu, J. Li, Z. Lin, Z. Chen, J. P. Matinlinna, Y. Zheng, S. Wu, X. Liu, K.P. Lai, Z. Chen, Y.W. Lam, K.M.C. Cheung, K.W.K. Yeung, TRPM7 kinase-mediated immunomodulation in macrophage plays a central role in magnesium ion-induced bone regeneration, Nat. Commun. 12 (2021) 2885.
[32] Z. Lin, D. Shen, W. Zhou, Y. Zheng, T. Kong, X. Liu, S. Wu, P.K. Chu, Y. Zhao, J. Wu, K.M.C. Cheung, K.W.K. Yeung, Regulation of extracellular bioactive cations in bone tissue microenvironment induces favorable osteoimmune conditions to accelerate in situ bone regeneration, Bioact. Mater. 6 (2021) 2315–2330.
[33] Z.Y. Zhang, Y.L. An, X.S. Wang, L.Y. Cui, S.Q. Li, C.B. Liu, Y.H. Zou, F. Zhang, R. C. Zeng, In vitro degradation, photo-dynamic and thermal antibacterial activities of Cu-bearing chlorophyllin-induced Ca-P coating on magnesium alloy AZ31, Bioact. Mater. 18 (2022) 284–299.
[34] J. Dong, W. Zhou, X. Hu, J. Bai, S. Zhang, X. Zhang, L. Yu, P. Yang, L. Kong, M. Liu, X. Shang, Z. Su, D. Geng, C. Zhu, Honeycomb-inspired ZIF-sealed interface enhances osseointegration via anti-infection and osteoimmunomodulation, Biomaterials 307 (2024) 122515.
[35] M. Nadeem, R. Khan, K. Afridi, A. Nadhman, S. Ullah, S. Faisal, Z.U. Mabood, C. Hano, B.H. Abbasi, Green synthesis of cerium oxide nanoparticles (CeO(2) NPs) and their antimicrobial applications: a review, Int J Nanomedicine 15 (2020) 5951–5961.
[36] Q. Maqbool, M. Nazar, S. Naz, T. Hussain, N. Jabeen, R. Kausar, S. Anwaar, F. Abbas, T. Jan, Antimicrobial potential of green synthesized CeO(2) nanoparticles from Olea europaea leaf extract, Int J Nanomedicine 11 (2016) 5015–5025.
[37] L. De Marzi, A. Monaco, J. De Lapuente, D. Ramos, M. Borras, M. Di Gioacchino, S. Santucci, A. Poma, Cytotoxicity and genotoxicity of ceria nanoparticles on different cell lines in vitro, Int. J. Mol. Sci. 14 (2013) 3065–3077.
[38] S. Khademolqorani, H. Tavanai, I.S. Chronakis, A. Boisen, F. Ajalloueian, The determinant role of fabrication technique in final characteristics of scaffolds for tissue engineering applications: a focus on silk fibroin-based scaffolds, Mater Sci Eng C Mater Biol Appl 122 (2021) 111867.
[39] T.B. Aigner, E. DeSimone, T. Scheibel, Biomedical applications of recombinant silk-based materials, Adv Mater 30 (2018) e1704636.
[40] V. Catto, S. Fare, I. Cattaneo, M. Figliuzzi, A. Alessandrino, G. Freddi, A. Remuzzi, M.C. Tanzi, Small diameter electrospun silk fibroin vascular grafts: mechanical properties, in vitro biodegradability, and in vivo biocompatibility, Mater Sci Eng C Mater Biol Appl 54 (2015) 101–111.
[41] J. Melke, S. Midha, S. Ghosh, K. Ito, S. Hofmann, Silk fibroin as biomaterial for bone tissue engineering, Acta Biomater. 31 (2016) 1–16.
[42] W. Zhang, L. Chen, J. Chen, L. Wang, X. Gui, J. Ran, G. Xu, H. Zhao, M. Zeng, J. Ji, L. Qian, J. Zhou, H. Ouyang, X. Zou, Silk fibroin biomaterial shows safe and effective wound healing in animal models and a randomized controlled clinical trial, Adv Healthc Mater 6 (2017).
[43] J. Yan, D. Xia, W. Zhou, Y. Li, P. Xiong, Q. Li, P. Wang, M. Li, Y. Zheng, Y. Cheng, pH-responsive silk fibroin-based CuO/Ag micro/nano coating endows polyetheretherketone with synergistic antibacterial ability, osteogenesis, and angiogenesis, Acta Biomater. 115 (2020) 220–234.
[44] L. Zhao, F. Zhang, X. Ding, G. Wu, Y.Y. Lam, X. Wang, H. Fu, X. Xue, C. Lu, J. Ma, L. Yu, C. Xu, Z. Ren, Y. Xu, S. Xu, H. Shen, X. Zhu, Y. Shi, Q. Shen, W. Dong, R. Liu, Y. Ling, Y. Zeng, X. Wang, Q. Zhang, J. Wang, L. Wang, Y. Wu, B. Zeng, H. Wei, M. Zhang, Y. Peng, C. Zhang, Gut bacteria selectively promoted by dietary fibers alleviate type 2 diabetes, Science 359 (2018) 1151–1156.
[45] C. Charlier, M. Cretenet, S. Even, Y. Le Loir, Interactions between Staphylococcus aureus and lactic acid bacteria: an old story with new perspectives, Int. J. Food Microbiol. 131 (2009) 30–39.
[46] H. Hemmatpour, O. De Luca, D. Crestani, M.C.A. Stuart, A. Lasorsa, P.C.A. van der Wel, K. Loos, T. Giousis, V. Haddadi-Asl, P. Rudolf, New insights in polydopamine formation via surface adsorption, Nat. Commun. 14 (2023).
[47] H. Lee, S.M. Dellatore, W.M. Miller, P.B. Messersmith, Mussel-inspired surface chemistry for multifunctional coatings, Science 318 (2007) 426–430.
[48] S. Asadpour, S. Kargozar, L. Moradi, A. Ai, H. Nosrati, J. Ai, Natural biomacromolecule based composite scaffolds from silk fibroin, gelatin and chitosan toward tissue engineering applications, Int. J. Biol. Macromol. 154 (2020) 1285–1294.
[49] X. Wang, L.S. Pan, A. Zheng, L.Y. Cao, J. Wen, T.S. Su, X.K. Zhang, Q.F. Huang, X. Q. Jiang, Multifunctionalized carbon-fiber-reinforced polyetheretherketone implant for rapid osseointegration under infected environment, Bioact. Mater. 24 (2023) 236–250.
[50] T. Zhao, X. Liu, Z. Chu, J. Zhao, D. Jiang, X. Dong, Z. Lu, K.W.K. Yeung, X. Liu, L. Ouyang, L-arginine loading porous PEEK promotes percutaneous tissue repair through macrophage orchestration, Bioact. Mater. 40 (2024) 19–33.
[51] Z. Yang, Y. Xi, J. Bai, Z. Jiang, S. Wang, H. Zhang, W. Dai, C. Chen, Z. Gou, G. Yang, C. Gao, Covalent grafting of hyperbranched poly-L-lysine on Ti-based implants achieves dual functions of antibacteria and promoted osteointegration in vivo, Biomaterials 269 (2021) 120534.
[52] S. Atefyekta, M. Pihl, C. Lindsay, S.C. Heilshorn, M. Andersson, Antibiofilm elastin-like polypeptide coatings: functionality, stability, and selectivity, Acta Biomater. 83 (2019) 245–256.
[53] A. Thill, O. Zeyons, O. Spalla, F. Chauvat, J. Rose, M. Auffan, A.M. Flank, Cytotoxicity of CeO2 nanoparticles for Escherichia coli. Physico-chemical insight of the cytotoxicity mechanism, Environ. Sci. Technol. 40 (2006) 6151–6156.
[54] A. Arumugam, C. Karthikeyan, A.S. Haja Hameed, K. Gopinath, S. Gowri, V. Karthika, Synthesis of cerium oxide nanoparticles using Gloriosa superba L. leaf extract and their structural, optical and antibacterial properties, Mater Sci Eng C Mater Biol Appl 49 (2015) 408–415.
[55] L. Jin, X. Liu, Y. Zheng, Y. Zhang, Z. Li, S. Zhu, H. Jiang, Z. Cui, S. Wu, Interfacial and defect polarization enhanced microwave noninvasive therapy for Staphylococcus aureus-infected chronic osteomyelitis, ACS Nano 17 (2023) 18200–18216.
[56] B.C. Heng, Y. Bai, X. Li, L.W. Lim, W. Li, Z. Ge, X. Zhang, X. Deng, Electroactive biomaterials for facilitating bone defect repair under pathological conditions, Adv. Sci. 10 (2023) e2204502.
[57] N.A. Hodges, E.M. Sussman, J.P. Stegemann, Aseptic and septic prosthetic joint loosening: impact of biomaterial wear on immune cell function, inflammation, and infection, Biomaterials 278 (2021) 121127.
[58] G.N. Duda, S. Geissler, S. Checa, S. Tsitsilonis, A. Petersen, K. Schmidt-Bleek, The decisive early phase of bone regeneration, Nat. Rev. Rheumatol. 19 (2023) 78–95.
[59] B. Xiao, Y. Liu, I. Chandrasiri, E. Adjei-Sowah, J. Mereness, M. Yan, D.S.W. Benoit, Bone-targeted nanoparticle drug delivery system-mediated macrophage modulation for enhanced fracture healing, Small 20 (2024) e2305336.
[60] M.L. Novak, T.J. Koh, Macrophage phenotypes during tissue repair, J. Leukoc. Biol. 93 (2013) 875–881.
[61] O.R. Mahon, D.C. Browe, T. Gonzalez-Fernandez, P. Pitacco, I.T. Whelan, S. Von Euw, C. Hobbs, V. Nicolosi, K.T. Cunningham, K.H.G. Mills, D.J. Kelly, A. Dunne, Nano-particle mediated M2 macrophage polarization enhances bone formation and MSC osteogenesis in an IL-10 dependent manner, Biomaterials 239 (2020) 119833.
[62] P. Miossec, J.K. Kolls, Targeting IL-17 and TH17 cells in chronic inflammation, Nat. Rev. Drug Discov. 11 (2012) 763–776.
[63] A. Beringer, P. Miossec, Systemic effects of IL-17 in inflammatory arthritis, Nat. Rev. Rheumatol. 15 (2019) 491–501.
[64] J.T. Niu, Y. Guo, G.X. Jing, H. Wang, L. Yang, Y.Y. Li, Y. Gao, H.C. Wang, A. Li, X. R. Xu, Y.C. Qian, J. Fei, S.L. Wang, Anion-Dependent layered double hydroxide nanoparticles regulate differentiation of CD206 CX3CR1 macrophages by inhibiting the IL-17 signaling pathway contributing to inflammatory bowel disease, Adv. Funct. Mater. 34 (2024).
[65] J.M. Sadowska, F. Wei, J. Guo, J. Guillem-Marti, Z. Lin, M.P. Ginebra, Y. Xiao, The effect of biomimetic calcium deficient hydroxyapatite and sintered beta-tricalcium phosphate on osteoimmune reaction and osteogenesis, Acta Biomater. 96 (2019) 605–618.
[66] B. Li, F. Liu, J. Ye, X. Cai, R. Qian, K. Zhang, Y. Zheng, S. Wu, Y. Han, Regulation of macrophage polarization through periodic photo-thermal treatment to facilitate osteogenesis, Small 18 (2022) e2202691.
[67] L. Yu, Y.S. Qiao, G.R. Ge, M. Chen, P. Yang, W.H. Li, Y. Qin, W.Y. Xia, C. Zhu, G. Q. Pan, P. Zhang, H.L. Yang, C. Wang, J.X. Bai, D.C. Geng, Rational Design of Engineered Bionic Periosteum for Dynamic Immunoinduction, Smart Bactericidal, and Efficient Bone Regeneration, Advanced Functional Materials (2024) 2401109.
[68] S. Jin, J. Gao, R. Yang, C. Yuan, R. Wang, Q. Zou, Y. Zuo, M. Zhu, Y. Li, Y. Man, J. Li, A baicalin-loaded coaxial nanofiber scaffold regulated inflammation and osteoclast differentiation for vascularized bone regeneration, Bioact. Mater. 8 (2022) 559–572.
[69] D.N. Rockwood, R.C. Preda, T. Yucel, X. Wang, M.L. Lovett, D.L. Kaplan, Materials fabrication from Bombyx mori silk fibroin, Nat. Protoc. 6 (2011) 1612–1631.